Dynamics of forecast-error growth along cut-off Sanchez and its consequence for the prediction of a high-impact weather event over southern France

Hanin Binder, Gwendal Rivière, Philippe Arbogast, Karine Maynard, Pierre Bosser, Bruno Joly, Carole Labadie

Received: 10 June 2021 | Accepted: 11 July 2021 | Published on: 19 August 2021

DOI: 10.1002/qj.4127

Quarterly Journal of the Royal Meteorological Society RMetS

RESEARCH ARTICLE

Dynamics of forecast-error growth along cut-off *Sanchez* and its consequence for the prediction of a high-impact weather event over southern France

Hanin Binder[1,2] | **Gwendal Rivière**[1] | **Philippe Arbogast**[3] | **Karine Maynard**[3] | **Pierre Bosser**[4] | **Bruno Joly**[3] | **Carole Labadie**[3]

[1]LMD/IPSL, ENS, PSL Université, École Polytechnique, Institut Polytechnique de Paris, Sorbonne Université, CNRS, Paris, France

[2]Institute for Atmospheric and Climate Science, ETH Zurich, Zurich, Switzerland

[3]CNRM/GAME, Météo-France/CNRS, Toulouse, France

[4]Lab-STICC UMR CNRS 6285/PRASYS, ENSTA Bretagne, Brest, France

Correspondence
H. Binder, Institute for Atmospheric and Climate Science, ETH Zurich, Universitätstrasse 16, CH-8092 Zurich, Switzerland.
Email: hanin.binder@env.ethz.ch

Funding information
Swiss National Science Foundation (SNSF), Grant/Award Numbers: 175161, 185049; French National Research Agency, Grant/Award Number: ANR-17-CE01-0010

Abstract

The representation of a high-impact weather (HIW) event over southern France is evaluated in Météo-France forecasts, and the sensitivity of the HIW forecast to the upstream upper-level flow and the Mediterranean and North Atlantic humidity structure prior to the event is quantified. The event occurred in October 2016 during the international field experiment NAWDEX. The approach of an upper-level potential vorticity (PV) cut-off, referred to as cut-off *Sanchez*, triggered extreme precipitation over southern France. Many 2- to 7-day ensemble forecasts predicted the maximum of the extreme precipitation and the location of the upper-level PV cut-off too far to the east. This eastward shift primarily resulted from an underestimation of the cut-off intensity two days before the HIW and the subsequent downstream propagation and amplification of these errors in the vicinity of *Sanchez*. Improving the representation of the cut-off two days before the event significantly improved the forecast quality. Another error source were inaccuracies in the moisture structure in the eastern North Atlantic. Specifically, an underestimation of the moisture in the warm conveyor belt inflow led to errors in the low- and upper-level circulation that eventually contributed to the eastward shift of the HIW two days later. Corrections in the eastern North Atlantic humidity structure further improved the forecast quality. On the other hand, corrections in the Mediterranean humidity structure had only a small impact on the accuracy of the forecast. The findings illustrate the importance of downstream error propagation and moist diabatic processes for the prediction of extreme weather over Europe, and demonstrate how targeted changes in the PV and humidity field a few days in advance can improve the quality of the forecasts.

KEYWORDS

diabatic processes, dynamics, forecast sensitivity, forecast verification, high-impact weather, humidity, NAWDEX, numerical weather prediction

1 | INTRODUCTION

Midlatitude extreme weather events like heavy precipitation and intense winds have a major social, environmental and economic impact (e.g., Wernli *et al.*, 2002; Rivière *et al.*, 2010; Grams *et al.*, 2014). Despite a continuous improvement in the skill of short- and medium-range weather forecasts in recent decades (e.g., Bauer *et al.*, 2015), the prediction of such high-impact weather (HIW) events continues to be a great challenge (Doyle *et al.*, 2014; Hewson *et al.*, 2014). In the western Mediterranean and over central Europe, HIW is often linked to the approach of a short-wave trough at the tropopause level, a so-called potential vorticity (PV) streamer (e.g., Massacand *et al.*, 1998; Martius *et al.*,2006; 2008; Nuissier *et al.*, 2011; Wirth *et al.*, 2018). PV streamers are meridionally elongated, narrow stratospheric intrusions of high PV. They destabilise the underlying air and, when present over western Europe, they induce the steady advection of warm and moist air from the nearby oceans toward the southern slope of the Pyrenees, the Massif Central or the Alps. The air is forced to rise as it impinges upon the topography, leading to orographically enhanced precipitation, often accompanied by flash floods.

Several studies indicate that inaccuracies in the representation of the upper-level PV streamers in numerical weather prediction (NWP) models can lead to forecast errors of the HIW at the surface. For instance, Fehlmann and Quadri (2000) and Schlemmer *et al.* (2010) showed that the forecast quality of heavy precipitation on the Alpine south-side depends on the mesoscale structure of the associated upper-level PV streamer. For an extreme precipitation and wind gust event over the western Mediterranean, Argence *et al.* (2009) revealed that small modifications in the upper-level PV structure substantially improved the forecast of the storm. Although it has been indicated that the predictive skill of large-scale flow conditions conducive for Alpine extreme precipitation is better than the skill of average flow conditions (Grazzini, 2007), errors in the representation of upper-level Rossby waves and the tropopause structure are still common in current NWP models (e.g., Davies and Didone, 2013; Gray *et al.*, 2014; Giannakaki and Martius, 2016). Such errors can arise, for instance, from errors in the representation of diabatic processes (Rodwell *et al.*, 2013; Martínez-Alvarado *et al.*, 2016).

In midlatitudes, intense diabatic processes occur in so-called warm conveyor belts (WCBs; e.g., Harrold, 1973; Wernli and Davies, 1997; Madonna *et al.*, 2014b; Binder *et al.*, 2016). WCBs are moist ascending airstreams in extratropical cyclones which are responsible for widespread cloud bands and strong precipitation (Browning, 1990). The latent heat release leads to the generation of negative PV anomalies in the tropopause region, which can amplify ridges and promote the formation and intensification of stratospheric PV streamers (Massacand *et al.*, 2001; Grams *et al.*, 2011; Madonna *et al.*, 2014a). Inaccuracies in the representation of WCBs, for instance due to errors in the initial moisture distribution in the WCB inflow (Schäfler *et al.*, 2011; Schäfler and Harnisch, 2015) or the representation of cloud microphysical processes (Joos and Forbes, 2016), can lead to errors in the location and structure of the tropopause. The initially localised, small-scale errors can grow rapidly to the synoptic scale (e.g., Davies and Didone, 2013; Martínez-Alvarado *et al.*, 2016; Baumgart *et al.*, 2018) and eventually affect the forecast skill of the downstream weather (Grams *et al.*, 2018).

The accurate prediction of heavy precipitation in the western Mediterranean region also depends on the representation of the initial moisture field (Ducrocq *et al.*, 2002) and the Mediterranean sea surface temperature (Lebeaupin *et al.*, 2006). The origin of the moisture feeding Mediterranean heavy precipitation events depends on the synoptic situation and includes local and remote sources. Duffourg and Ducrocq (2011; 2013) estimated that, with anticyclonic conditions prevailing, about 60% of the moisture is provided by evaporation from the Mediterranean Sea within the 2 days preceding the event, while the remaining moisture originates from remote sources over the North Atlantic or North Africa. During cyclonic conditions, the contribution from remote sources is larger, with about 45% coming from the North Atlantic and 15% from North Africa, while the contribution from local Mediterranean sources decreases to about 40%. The importance of North Atlantic moisture for Mediterranean extreme precipitation was also shown by Turato *et al.* (2004) and Winschall *et al.* (2012). For a heavy precipitation event in the Piedmont region in November 2002, Winschall *et al.* (2012) revealed the key role of an evaporation hot spot occurring 1–4 days prior to the event about 2,000 km upstream in the eastern North Atlantic. The strong evaporation was induced by a northerly low-level flow to the west of an upper-level trough, and the evaporated moisture was subsequently advected around the trough and into the Mediterranean, where it contributed to the HIW event.

The densely populated Mediterranean basin is one of the most vulnerable regions in the world to natural hazards (Hinrichsen, 1998; Ducrocq *et al.*, 2014) and extremely sensitive to global climate change (Giorgi, 2006). An increased understanding of the dynamics and forecast performance of extreme events in this region is crucial to improve forecasting and warning capabilities. The aim of this study is to evaluate the representation of a Mediterranean HIW event and the associated upper-level flow structure in probabilistic and deterministic forecasts from the Météo-France global operational model Action

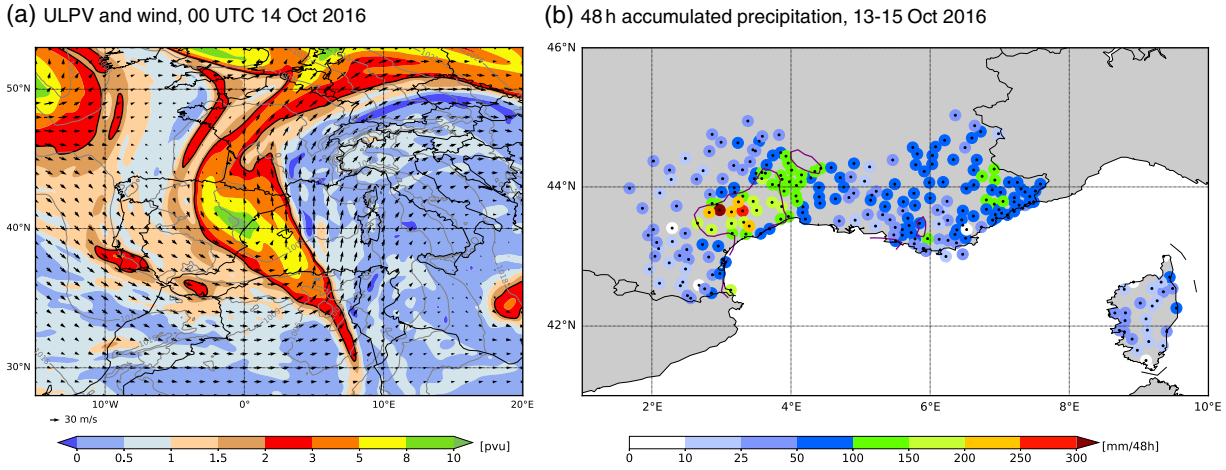

FIGURE 1 HIW event over southern France on 13–14 October 2016. (a) 320–330 K vertically averaged PV (pvu; colour shading) and wind vectors ($m \cdot s^{-1}$; arrows) at 0000 UTC on 14 October 2016 from ARPEGE operational analyses, and (b) Météo-France raingauge observations of 48 hr accumulated precipitation between 0000 UTC 13 October and 0000 UTC 15 October 2016 (mm; coloured dots), and 50 mm contour (purple) of 12 hr accumulated precipitation between 1800 UTC 13 October and 0600 UTC 14 October 2016 [Colour figure can be viewed at wileyonlinelibrary.com]

de Recherche Petite Echelle Grande Echelle (ARPEGE; Courtier *et al.*, 1991), and to assess how changes in the upper-level PV and low-level moisture structure in specific target regions a few days prior to the event can affect the quality of the forecasts. To this end, we focus on an extreme precipitation event over southern France that occurred on 13/14 October 2016 during the North Atlantic Waveguide and Downstream Impact Experiment (NAWDEX; Schäfler *et al.*, 2018). The HIW was triggered by an upper-level PV cut-off, referred to as PV cut-off *Sanchez*, which propagated eastward from the North Atlantic into the Mediterranean and eventually transformed into a PV streamer (Figure 1a). Ahead of the streamer in the department of Hérault over southern France, more than 300 mm of precipitation fell within two days (Figure 1b), and wind gusts of about 100 $km \cdot hr^{-1}$ were experienced (Schäfler *et al.*, 2018). Based on objective verification techniques and PV inversion and moisture replacement experiments, we address the following questions:

1. How well are the extreme precipitation event over southern France on 13/14 October 2016 and the associated upper-level PV streamer represented in a state-of-the-art NWP model?
2. Is the forecast quality of the HIW linked to the forecast quality of PV streamer *Sanchez*?
3. Is the HIW event sensitive to the representation of (a) the upstream upper-level flow, and (b) the North Atlantic or Mediterranean humidity structure at earlier times?

The ARPEGE model used in this study is not convection-permitting, so we do not focus on the convective-scale structure of potential forecast errors, but on their representation on the scale of a few 100 km. The article is organised as follows. In Section 2, we describe the data and methods used. The representation of the HIW event in ensemble data is discussed in Section 3. Section 4 investigates the sensitivity of the event to the upper-level PV and low-level moisture two days earlier in deterministic forecasts, based on PV inversion and moisture experiments. A summary of the results and the main conclusions are provided in Section 5.

2 | DATA AND METHODS

2.1 | Probabilistic and deterministic forecasts

The study is based on data from the global operational Météo-France model ARPEGE (Courtier *et al.*, 1991). Initial conditions were provided by a 4D-Var data assimilation scheme in which the background-error covariance matrix is sampled by an ensemble of data assimilations. Probabilistic and deterministic forecasts are discussed. The probabilistic dataset used the model uncertainties package of the Météo-France global operational short-range ensemble prediction system PEARP (Prévision d'Ensembles ARPege; Descamps *et al.*, 2015) and is an adapted version of the reforecast datasets described in Boisserie *et al.* (2016a; 2016b) and Ponzano *et al.* (2020). It consists of ten ensemble members run four times daily for 7 days. All members were initialised with ARPEGE operational analyses, that is, they did not differ in terms of initial conditions. Each member was associated with a different set of physical parametrizations to represent model

uncertainties associated with shallow and deep convection, turbulence and oceanic fluxes – the same as used in Ponzano *et al.* (2020). Deep convection was parametrized by two different mass flux schemes, the Bougeault (1985) scheme and the Prognostic Condensates Microphysics and Transport (PCMT) scheme (Piriou *et al.*, 2007). For the parametrization of shallow convection, four different schemes were used: the PCMT scheme, a mass-flux scheme based on Kain and Fritsch (1993) and modified by Bechtold *et al.* (2001), the eddy diffusivity and Kain and Fritsch (1993) scheme and the PMMC scheme (Pergaud *et al.*, 2009). Ensemble member 0 used the same combination of parametrizations as the operational deterministic ARPEGE simulation at the time of the HIW event; it differs from the operational simulation only in terms of resolution. The horizontal spectral truncation of the ensemble forecasts was T798 on 90 vertical levels with a mapping factor of 2.4 (i.e., about 10 km horizontal resolution over France and 60 km on the opposite side of the globe). The time step was 450 s and the output fields were produced every 6 hr. The original fields were interpolated onto a regular grid with 0.5° horizontal resolution.

Deterministic ARPEGE forecasts were used to perform sensitivity experiments. They were run at a spatial resolution of T1198 with a mapping factor of 2.2 (i.e., 7.5 km over France and 37 km at the antipode) on 105 vertical levels, with the first level at 10 m above the surface and the uppermost level at around 70 km. The time step was 360 s and the output fields were produced every hour. The fields were investigated on a regular horizontal grid with 0.1° resolution. Deep convection was parametrized as in Bougeault (1985). The modification of the initial state of the experiments is described in Section 2.3.

2.2 | Forecast verification

For each ensemble member, the anomaly correlation coefficient (ACC) was calculated for vertically averaged PV between 320 and 330 K and 12 hr accumulated precipitation over southern France (1°–10°E, 41°–46°N). Both quantities were evaluated in the middle of the HIW event, upper-level PV at 0000 UTC on 14 October 2016, and precipitation in the 12 hr window between 1800 UTC 13 October and 0600 UTC 14 October 2016. The anomalies of the forecasts and the verifying fields were computed with respect to the ERA-Interim-based climatological mean for autumn 1979–2016 (Dee *et al.*, 2011). The ACC is a broad measure of forecast quality that lies between −100 and +100%, with values below 60% commonly regarded as indicating poor forecast skill (Wilks, 2006). It is a gridpoint-based metric which is particularly appropriate for the verification of synoptic-scale flow features. However, for precipitation, which is strongly variable on small spatial and temporal scales, the ACC alone is not suitable. In particular, one limitation of the ACC and other gridpoint-based metrics is that they score badly when a predicted weather system is (slightly) misplaced, even if the amplitude, structure and timing are correct (this is referred to as the "double penalty problem"; e.g., Davis *et al.*, 2006; Wernli *et al.*, 2008).

Therefore, precipitation errors were additionally quantified with the three-component feature-based SAL technique (Wernli *et al.*, 2008) which allows us to evaluate separately the structure (S), amplitude (A) and location (L) of precipitation objects within a target domain. The verification domain is the same as for the ACC, that is 1°–10°E, 41°–46°N. The amplitude component compares the domain-averaged precipitation between the observed and predicted fields. It is defined such that it lies between −2 and +2, with 0 indicating perfect forecasts, positive values an overestimation and negative values an underestimation of total precipitation. For the calculation of the location and structure components, precipitation objects were identified in the observed and forecast fields based on a threshold value. We used the same threshold R as in Wernli *et al.* (2009), that is, $R = R^{95}/15$, where R^{95} denotes the 95th percentile of all grid-point values with precipitation larger than 0.1 mm. The location component provides information about the displacement between the predicted and observed centres of mass of the precipitation objects. It ranges from 0 to 2, with 0 indicating a perfect forecast. Finally, the structure component gives insight into the shape and size of the precipitation objects. It ranges from −2 to +2, with 0 again representing perfect forecasts. Positive values indicate too large and/or too flat forecasted precipitation objects, and negative values indicate too small and/or too peaked objects (Wernli *et al.*, 2008 give details).

The upper-level PV forecasts were verified against ARPEGE operational analyses, and precipitation against the ensemble mean of the forecasts at 6 hr lead time, since ARPEGE does not include analysis data for precipitation. Compared to rain gauge observations, using short-term precipitation forecasts as reference data has the advantage that the values are representative for the same grid scales as the verified forecast data, and that the validation is also possible over the ocean. On the other hand, one disadvantage is that the 6 hr precipitation forecasts when used as reference data share the same model deficiencies as the longer-term forecasts we want to evaluate, such as under-resolved topography and errors in the microphysics and convective schemes. For the HIW event investigated in this study, the 6 hr precipitation forecasts do not vary strongly among the ten different ensemble members, so that choosing the ensemble mean, median or a single

member as the reference dataset has little impact on the results.

In the deterministic forecasts, the moisture structure was verified by comparing the modelled integrated water vapour (IWV) with IWV retrievals from Global Positioning System (GPS) measurements at different continuously operating European Global Navigation Satellite System (GNSS) stations (Bosser and Bock, 2021). Zenith tropospheric delays (ZTDs) were estimated at 5 min intervals to correct the delays that occur during the propagation of GPS signals through the troposphere. These delays depend on humidity. ZTDs were then converted into IWV using surface pressure from ARPEGE operational analyses and mean atmospheric temperature from grid values provided by the TU-Wien database (https://vmf.geo.tuwien.ac.at, accessed 20 June 2020), following the same methodology as in Bosser and Bock (2021). In the present study, we used IWV retrievals from 456 stations over western Europe located between 10°W–15°E and 35°–50°N and available at full hours between 0000 UTC 12 October and 0000 UTC 14 October 2016. The root-mean-square error (RMSE) and the bias (model minus observation) of the predicted with respect to the observed values were calculated based on bilinear interpolation. Note that ARPEGE assimilates IWV retrievals from GNSS data which are produced in near-real time; but in the present study the GNSS dataset is based on a denser network and a different, more accurate retrieval method than the assimilated data. In particular, the current retrieval has been produced with an improved processing procedure with more accurate models and final GPS satellite orbit and clock products. (Bock *et al.*, 2016 show an evaluation of a near-real-time dataset with respect to a post-processed dataset.) Hence, although the model and the verified data might not be completely independent, the different networks and retrieval methods allow for a meaningful comparison between the two datasets.

2.3 | PV inversion and moisture replacement algorithms

To investigate the impact of local PV and moisture modifications on the HIW forecasts, numerical experiments were performed using the deterministic version of ARPEGE operational at the time of the event (Section 2.1). The sensitivity of the HIW to the upper-level PV cut-off was studied with the Ertel PV inversion algorithm of Arbogast *et al.* (2008) and a digital filter procedure used as an implicit balance condition (Arbogast *et al.*, 2012). For the lower boundary of the inversion, we chose the model level closest to 850 hPa, which is considered to be the top of the boundary layer. A Dirichlet boundary condition was used with mean sea level pressure as a proxy for the 850 hPa geopotential height through a simple linear regression (Arbogast *et al.*, 2008 give details). In what follows, the PV inversion tool was applied to modify the upper-level PV of a given state in specific target regions to build a new state with modified wind, temperature and geopotential height fields which serve as the initial state of a new simulation. Different PV modifications were set up and all of them were restricted to the layer between 100 hPa and 600 hPa. This led to different initial states and numerical experiments (Section 4 and Table 1 give detailed descriptions of the experiments). The PV inversion tool has already been used in process studies of North Atlantic wind storms (Rivière *et al.*, 2010; Rivière *et al.*, 2012) and of a Mediterranean cyclone that led to a heavy precipitation event (Argence *et al.*, 2009). Its application in an operational context has been discussed in Arbogast *et al.* (2012).

To study the sensitivity of the HIW to the North Atlantic and Mediterranean moisture structure, a second set of experiments was created where moisture modifications were applied over a specific target region in the lower and middle troposphere, similar to the approach described in Fresnay (2014). The moisture modifications were introduced following a simple procedure: the 3D specific humidity field of a given state was modified by another model state in a cube delimited by the 1,010–500 hPa layer in the vertical and a chosen horizontal domain. There is no particular procedure to deal with potential discontinuities at the boundaries of the chosen horizontal domain. The other variables were not modified. In particular, the temperature remained unaltered, so that the procedure did not consider any adjustment to saturation. The discontinuities and potential incoherences between the variables introduced in the initial conditions were smoothed out during the first hours of the model simulations.

2.4 | PV error tendency equation

The growth of PV errors (PV*) at the tropopause was investigated with the PV error tendency equation of Davies and Didone (2013). It describes the PV error evolution on an isentropic surface, which takes the following form (also Baumgart *et al.*, 2018):

$$\left(\frac{\mathrm{DPV^*}}{\mathrm{D}t}\right)_{\mathrm{ref}} = \underbrace{-\,\mathbf{v^*}\cdot\nabla_\theta \mathrm{PV}_{\mathrm{ref}}}_{\text{Term 1}} \underbrace{-\,\mathbf{v^*}\cdot\nabla_\theta \mathrm{PV^*}}_{\text{Term 2}} + \mathrm{NonCons^*} + \mathrm{Res^*}. \quad (1)$$

Here, the operator $\mathrm{D/Dt_{ref}}$ denotes the horizontal part of the material derivative following the flow of the reference field (subscript ref):

$$\left(\frac{\mathrm{D}}{\mathrm{D}t}\right)_{\mathrm{ref}} = \left(\frac{\partial}{\partial t}\right)_\theta + (\mathbf{v}_{\mathrm{ref}}\cdot\nabla_\theta), \quad (2)$$

where the subscript θ indicates derivatives evaluated on constant isentropic surfaces, and $\mathbf{v} = (u, v)$ is the horizontal wind. The index * indicates forecast errors, which are defined as the difference between the forecast (subscript fc) and the reference field, that is, PV*=$PV_{fc}-PV_{ref}$, and $\mathbf{v}^* = \mathbf{v}_{fc} - \mathbf{v}_{ref}$.

The first term on the right-hand side of Equation (1) describes the growth of an air parcel's PV error via isentropic advection of the PV field of the reference flow by the isentropic wind errors. The second term refers to nonlinear PV error growth via isentropic advection of the PV error field by the isentropic wind errors. NonCons* corresponds to errors associated with non-conservative processes like diabatic heating and friction, and Res* is the residual error arising due to numerical diffusion and various computational approximations like interpolation and discretisation of the data .

With the presence of Eulerian datasets of the meteorological variables both for the reference and the forecasted flow, Equation (1) can be computed by calculating isentropic backward trajectories from a specific region with high PV errors and tracing PV*, term 1 and term 2 along them from the Eulerian datasets. This allows us to gain insight into the processes contributing to the growth of the PV error. $(DPV^*/Dt)_{ref}$ can be approximated by the change in PV* along the trajectories within the time interval Δt, denoted as $(DPV^*/Dt)_{ref} \approx (\Delta PV^*/\Delta t)_{ref}$. In the present study, Δt corresponds to 1 hr. We do not calculate non-conservative processes explicitly, but derive them, together with the residue, from the other terms, that is,

$$\text{NonCons*} + \text{Res*} = \left(\frac{\Delta \text{PV*}}{\Delta t}\right)_{\text{ref}} \underbrace{+\mathbf{v^*} \cdot \nabla_\theta \text{PV}_{\text{ref}}}_{\text{Term 1}} \underbrace{+\mathbf{v^*} \cdot \nabla_\theta \text{PV*}}_{\text{Term 2}}. \quad (3)$$

2.5 | WCB trajectory calculation

For the numerical experiments, WCB trajectories were computed following the approach of Madonna *et al.* (2014b). Two-day forward trajectories were started with the Lagrangian Analysis Tool (LAGRANTO; Wernli and Davies, 1997; Sprenger and Wernli, 2015) from an equidistant grid with 40 km horizontal and 25 km vertical resolution between 1000 and 700 hPa. Trajectories with an ascent of more than 600 hPa in two days are considered as WCB trajectories. In contrast to Madonna *et al.* (2014b), the WCB trajectories are not required to overlap with an extratropical cyclone during their ascent.

3 | REPRESENTATION OF THE EVENT IN ENSEMBLE FORECASTS

Figure 2a shows for different lead times the forecast quality of upper-level PV over southern France at 0000 UTC 14 October 2016 in terms of the ACC, separately for the ensemble mean and each ensemble member. It lies between 70 and 90% for 1–3 day forecasts, decreases to 40–80% for 3–4 day forecasts, and drops to poor values below 0% for many forecasts with lead times beyond 4 days. The ensemble mean (black line) has a higher skill than most ensemble members, in particular for 1–4 day lead times. The ACC of precipitation accumulated over southern France between 1800 UTC 13 October and 0600 UTC 14 October 2016 (Figure 2b) shows a similar dependency on lead time[1], suggesting a link between the representation of precipitation and upper-level PV. However, for 1–4 day forecasts, the spread between the ensemble members is larger and the skill generally lower than for PV, with most values between 40 and 80%. For forecasts beyond 4 days lead time, the ACC drops again to very poor skills around 0%.

An assessment of the forecast quality of precipitation in terms of the feature-based measure SAL is given in Figure 2c. Each ensemble member of the 1–7 day forecasts corresponds to one entry in the diagram, with circles indicating 1–4 day and squares 4.25–7 day forecasts. Ensemble mean values are highlighted with magenta symbol borders. Light blue circles in the centre of the diagram indicate very good forecasts in terms of all three components. Most 1–4 day forecasts, including the ensemble mean, are found in the second quadrant of the diagram (top left) and associated with a positive amplitude and a negative structure component, that is, they overestimate the amount of total precipitation in the domain and produce too small and/or too peaked precipitation objects. Further analyses (not shown) revealed that in these cases too intense convective showers are predicted, such that the negative structure error is associated with too peaked objects. The amplitude error is small to moderate, with the highest values around 0.5 indicating an overestimation of total precipitation by a factor of about 1.7. Some of the 1–4 day forecasts are also associated with relatively large location errors. Consistent with the drop in the ACC beyond 4 days lead time (Figure 2b), the errors in terms of S, A and L also increase strongly. Most of the 4.25–7 day forecasts are located in the third quadrant and associated with large negative amplitude and structure errors, that is, total precipitation

[1]For precipitation, lead time is defined as the time between the start of the forecast and 0000 UTC 14 October, that is, the middle of the 12 hr period of accumulated precipitation, such that it is consistent with the lead time for upper-level PV.

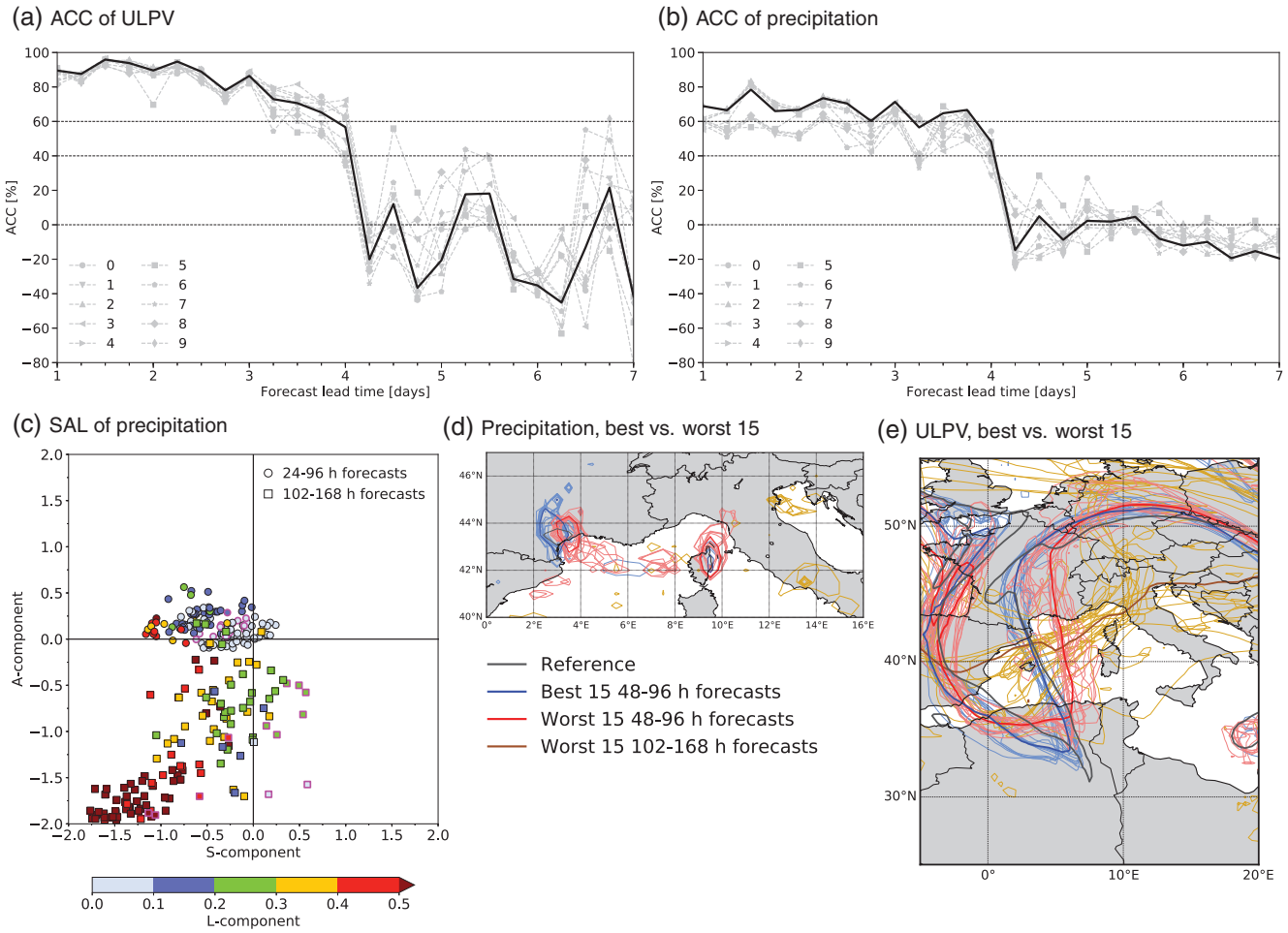

FIGURE 2 Representation of the HIW event in ARPEGE ensemble forecasts: (a) Anomaly correlation coefficient (ACC) of 320–330 K vertically averaged PV over southern France (1°–10°E, 41°–46°N) at valid time 0000 UTC 14 October 2016 as a function of forecast lead time. The black line shows the ensemble mean and the grey lines the individual ensemble members. (b) is as (a), but for the ACC of 12 hr accumulated precipitation between 1800 UTC 13 October and 0600 UTC 14 October 2016. (c) shows the SAL diagram of 12 hr accumulated precipitation over southern France (same area as (a)) between 1800 UTC 13 October and 0600 UTC 14 October 2016 for all 6-hourly ensemble forecasts with lead times of 1–4 days (i.e., 24–96 hr; circles) and 4.25–7 days (i.e., 102–168 hr; squares). Magenta symbol borders mark ensemble mean values for a given lead time. (d) shows the 50 mm contour of 12 hr accumulated precipitation of the best 15 2–4 day forecasts (blue), the worst 15 2–4 day forecasts (red) and the worst 15 4.25–7 day forecasts (brown) in terms of the ACC of precipitation (thin lines for the individual members and thick line for the mean), together with the reference dataset (black). (e) shows the associated 2 pvu contour of the 320–330 K vertically averaged PV

is too weak and the objects are again too peaked and/or too small. In addition, the colours indicate large errors in the position of the precipitation. Additional analyses of these members showed that they typically predict very little precipitation in the considered domain, but have their maximum farther to the east outside the domain (not shown).

To get further insight into the precipitation structure of particularly good and bad forecasts, Figure 2d shows the 50 mm contour of the 15 best 2–4 day forecasts (blue; mean lead time of 62 hr), the 15 worst 2–4 day forecasts (red; mean lead time of 85 hr) and the 15 worst 4.25–7 day forecasts (brown; mean lead time of 128 hr) in terms of the ACC of precipitation, together with the reference dataset (black). An overestimation of the amplitude is evident both for the best and the worst 2–4 day forecasts, consistent with the findings from the SAL diagram. The most remarkable difference between the two clusters is the location of precipitation: in the 15 worst 2–4 day forecasts, the forecast precipitation maximum and the centre of mass are shifted slightly eastward with respect to the best 15 and the reference fields. For the prediction of HIW it is crucial to accurately capture the exact location of the event, so this eastward shift, which on average amounts

to about 100–200 km, denotes an important location error. The finding that the two clusters do not differ strongly in terms of the amplitude, but more in terms of the location of the predicted precipitation, is related to the fact that they are defined based on the ACC, which has particularly low scores for misplaced features (also Section 2.2). As discussed above, many ensemble members are also associated with considerable amplitude and structure errors (Figure 2c) and, although they are also important, we focus only on the location errors in the following. In the worst 4.25–7 day forecasts, these location errors are even more pronounced, with no precipitation occurring over southern France, but some smaller maxima near Rome and over northeastern Italy (Figure 2d).

The eastward shift in precipitation in the bad forecasts goes along with an eastward shift of the leading edge of the upper-level PV streamer (Figure 2e). In the worst 2–4 day forecasts, the leading edge is located about 200 km too far to the east with respect to the good forecasts and the analysis, and the streamer is broader and less elongated. This suggests a link between the errors in the representation of the extreme precipitation and those associated with the PV streamer. In the worst 4.25–7 day forecasts, the PV streamer is not captured at all, but only a weak disturbance is present between Spain and northern Italy.

To assess whether the eastward shift in the precipitation maximum and the leading edge of PV streamer *Sanchez* in the worst 2–4 day forecasts might be linked to upper-level errors at earlier forecast times, Figure 3a shows the difference in mean upper-level PV between the 15 worst and 15 best 2–4 day forecasts two days before the HIW event, at 0000 UTC 12 October 2016. *Sanchez* is still a cut-off at this time and located over the eastern North Atlantic. Over large parts of the cut-off, the PV values are lower in the bad than in the good forecasts (blue colours). This is also evident in the west–east vertical cross-section through the cut-off averaged over the latitudinal band between 39° and 51°N (Figure 3b). In addition to the cut-off, differences between the good and bad forecasts are also present in most other areas near the tropopause (Figure 3a). All these differences can potentially play a role for the errors in the representation of the HIW two days later (Figure 2d,e). In the following Section, we will isolate the differences associated with the cut-off to assess their sole impact on the HIW forecast. We hypothesize that these differences are the most important ones, as the cut-off is the precursor of the PV streamer. Note that the particularly bad 4.25–7 day forecasts (brown colours in Figure 2d,e) share much less of a common pattern than the bad 2–4 day forecasts and are already associated with a relatively large variability in the position of *Sanchez* two days before the HIW (not shown). In the following, these forecasts will not be discussed further.

4 | FORECAST SENSITIVITY TO THE UPPER-LEVEL PV AND LOW-LEVEL MOISTURE TWO DAYS BEFORE THE EVENT

4.1 | Control runs and experimental design

The above discussed differences in upper-level PV between the 15 best and 15 worst ensemble forecasts suggest a potential link between the lower PV values within large parts of cut-off *Sanchez* at 0000 UTC 12 October 2016 in the worst members and the eastward shift of the PV streamer and precipitation maximum over southern France two days later. To test this, in this Section we run a set of sensitivity numerical experiments with the deterministic Météo-France forecasting system. The forecast sensitivity to the upper-level PV two days before the event was assessed with PV inversion experiments. In addition, moisture replacement experiments were performed to test the forecast sensitivity to the low-level moisture in the North Atlantic and Mediterranean. We started from two control forecasts, a good one in terms of the forecast precipitation over southern France and the structure of the associated PV streamer *Sanchez* (referred to as $\mathrm{Ctrl_{Good}}$; it is representative for the 15 best ensemble forecasts), and a second one associated with relatively large forecast errors ($\mathrm{Ctrl_{Bad}}$; representative for the 15 worst 2–4 day ensemble forecasts). Both forecasts were initialised with operational analyses, $\mathrm{Ctrl_{Good}}$ at 0000 UTC 12 October 2016 and $\mathrm{Ctrl_{Bad}}$ 30 hr earlier, at 1800 UTC 10 October. In the bad run, the leading edge of the PV streamer and the maximum of the 12 hr accumulated precipitation over southern France on 14 October were forecast too far to the east relative to the good run (Figure 4a,f) and the analysed fields (not shown), consistent with the medium-large eastward shift observed for the poor 2–4 day ensemble forecasts (red contours in Figure 2d,e).

Two days before the HIW, at the initial time of $\mathrm{Ctrl_{Good}}$ at 0000 UTC 12 October, the PV values in the 30 hr forecast of $\mathrm{Ctrl_{Bad}}$ were lower than those in $\mathrm{Ctrl_{Good}}$ within large parts of the cut-off and most other stratospheric regions (compare Figure 5a,b and the difference between the two in Figure 5c). At this time, the fields in $\mathrm{Ctrl_{Good}}$ correspond to the operational analyses, such that the lower upper-level PV values in $\mathrm{Ctrl_{Bad}}$ can be regarded as negative errors with respect to the analysed fields. Even though the pattern at 320–330 K is not the same as that of the ensemble mean of the 15 worst members (compare Figure 5c and Figure 3a), the common feature is an overall underestimation of the cut-off intensity of the bad with respect to the good runs, which is even more pronounced in the difference between $\mathrm{Ctrl_{Bad}}$ and $\mathrm{Ctrl_{Good}}$ than in the difference

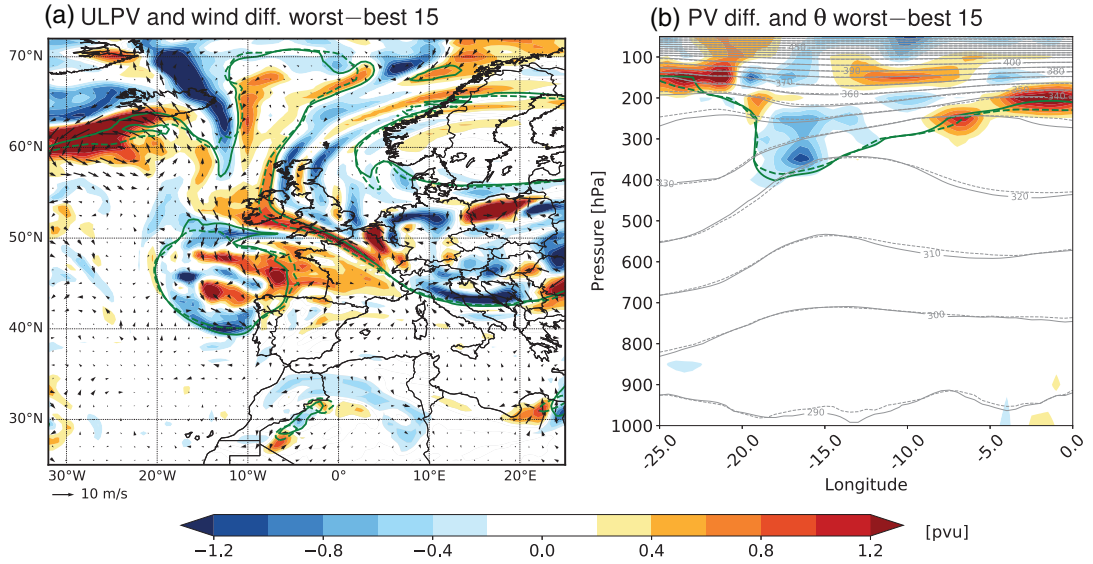

FIGURE 3 Difference between the mean fields of the worst 15 and the best 15 2–4 day ensemble forecasts two days before the HIW, at 0000 UTC 12 October 2016, in terms of (a) 320–330 K vertically averaged PV (pvu; shading) and wind ($m \cdot s^{-1}$; arrows), and (b) PV (pvu; shading) averaged in the latitudinal band between 39° and 51°N in a west–east vertical cross-section from 25°W to 0° longitude. The mean 2 pvu contour (green in (a) and (b)) and the mean potential temperature (grey in (b)) are shown as solid and dashed lines for the best and worst 15 ensemble members, respectively

between the two ensemble clusters. In the present article, the main goal is to understand the effect of these underestimated PV values on the forecast of the HIW rather than to interpret the underestimation. However, a brief analysis of the PV anomalies in Ctrl_{Bad} led us to the following conclusions. The negative errors in the centre of the cut-off in Ctrl_{Bad} are probably associated with too weak diabatic PV production by radiative cooling due to an underestimation of the relative humidity gradient below the cut-off (not shown). In contrast, the negative errors on its northeastern side appear to be related to an overestimation of the WCB ascent and upper-level diabatic PV erosion in that region.

In addition to the differences in the upper-level flow between $\text{Ctrl}_{\text{Good}}$ and Ctrl_{Bad} on 12 October, there are also differences in the moisture structure in the eastern North Atlantic and the Mediterranean (Figure 5d–f) which potentially contribute to the misrepresented HIW two days later. In both runs a filament with high moisture extends from the central North Atlantic to Portugal, but it is narrower and more elongated in the bad run (compare Figures 5d,e). This goes along with a complex error pattern in the IWV (Figure 5f) of Ctrl_{Bad} with respect to $\text{Ctrl}_{\text{Good}}$ (and accordingly with respect to the analysed fields), with predominantly negative errors (i.e., an underestimation of the moisture) at the northern and southeastern side and in the centre of the filament. Negative errors are also found in a second filament with increased IWV west of the cut-off. In contrast, in large parts of the Mediterranean the IWV is overestimated in Ctrl_{Bad}. A comparison of the two runs with IWV derived from GPS measurements at different western European stations during the two days leading to the HIW event confirms that the representation of the moisture structure is indeed worse in Ctrl_{Bad} than in $\text{Ctrl}_{\text{Good}}$ (Figure 6). At many stations, the RMSE over all hourly modelled values between 0000 UTC 12 October and 0000 UTC 14 October with respect to the observations is higher in Ctrl_{Bad}, in particular along the west coast of France, the south coast of Spain and in the region of the HIW event over southern France (Figure 6a,b), with a mean and standard deviation over all stations of $2.20 \pm 0.80\ \text{kg}\cdot\text{m}^{-2}$ in Ctrl_{Bad} versus $1.84 \pm 0.76\ \text{kg}\cdot\text{m}^{-2}$ in $\text{Ctrl}_{\text{Good}}$. Also the bias, which is negative in both models (i.e., the IWV is underestimated), is almost twice as large in Ctrl_{Bad} ($-0.67 \pm 1.08\ \text{kg}\cdot\text{m}^{-2}$) as in $\text{Ctrl}_{\text{Good}}$ ($-0.34 \pm 0.84\ \text{kg}\cdot\text{m}^{-2}$). The temporal evolution of the observed IWV at the station Tarifa in southern Spain (indicated by the black circle in Figure 6d,e) shows a fast increase between about 0600 and 1800 UTC on 12 October (red line in Figure 6c), which, as will be discussed later, is associated with the advection of the filament with high moisture from the Atlantic into the Mediterranean. The strong increase is fairly well captured in $\text{Ctrl}_{\text{Good}}$ (blue solid line in Figure 6c and map in Figure 6d), whereas in Ctrl_{Bad} the strong increase occurs about 3 hr too late (blue dashed line in Figure 6c), because the filament with high moisture is too narrow (Figure 6e).

In order to isolate the impact of the negative PV errors within the cut-off and the IWV errors in the different ocean basins on the HIW forecast two days later, several experiments will now be performed where the errors of Ctrl_{Bad}

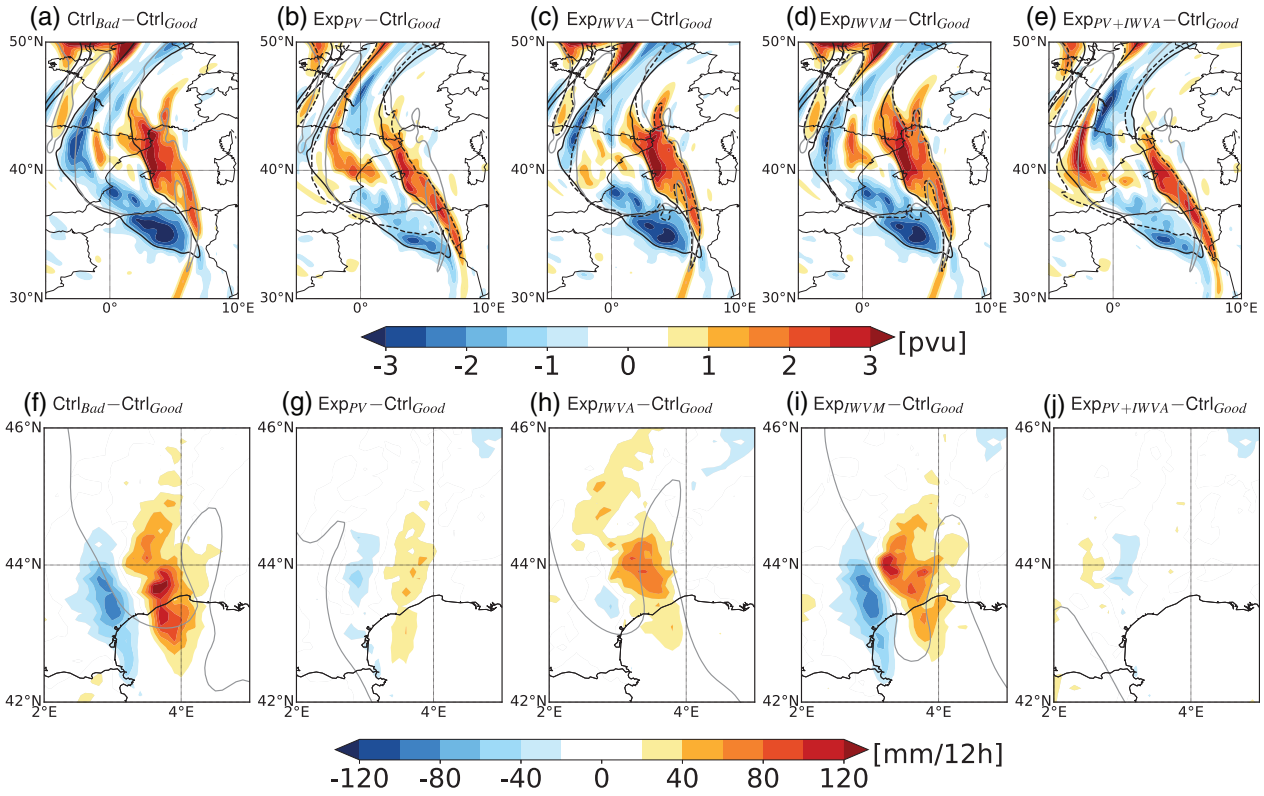

FIGURE 4 Upper-level PV and precipitation errors with respect to Ctrl$_{Good}$ at 0000 UTC 14 October 2016 in the deterministic forecasts. (a–e) 320–330 K vertically averaged PV error at 0000 UTC 14 October 2016 (pvu; shading) and (f–j) error of 12 hr accumulated precipitation between 1800 UTC 13 October and 0600 UTC 14 October 2016 (mm 12 hr^{-1}; shading) of (a, f) Ctrl$_{Bad}$, (b, g) Exp$_{PV}$, (c, h) Exp$_{IWVA}$, (d, i) Exp$_{IWVM}$, and (e, j) Exp$_{PV+IWVA}$. Overlaid is the 320–330 K averaged 2 pvu contour of Ctrl$_{Good}$ (black solid in a–e), Ctrl$_{Bad}$ (grey solid in a–f), and of the modified experiments (black dashed in b–e, grey solid in g–j)

with respect to the analysis will be removed locally. All experiments are initialised at 1800 UTC 10 October with the set-up of Ctrl$_{Bad}$, but after 30 hr lead time, at 0000 UTC 12 October, in a specific target region the forecast PV and/or IWV fields are replaced by the operational analyses (that is, the initial state of Ctrl$_{Good}$). If the errors in the target region are important for the misrepresented HIW, removing them in the numerical experiments should lead to improved forecasts. Table 1 provides an overview of the different experiments.

4.2 | Forecast sensitivity to the upper-level PV two days before the event

In the first experiment, Exp$_{PV}$, the upper-level PV of Ctrl$_{Bad}$ is replaced by the analysis in the region around cut-off *Sanchez* (at 25°–5°W, 35°–55°N, between 100 and 600 hPa), that is, the PV errors associated with the cut-off are minimized[2] (Figure 7a). This also goes along with a strong reduction in the upper-level wind errors in that region.

Figure 4b,g show that the PV modifications within the cut-off lead to a strong improvement in the representation of the PV streamer and the precipitation over southern France two days later. The forecast errors of Exp$_{PV}$ with respect to Ctrl$_{Good}$ (Figure 4b,g) are much smaller than those in the bad run (Figure 4a,f), with a strongly reduced eastward shift of both the PV streamer and the maximum of the 12 hr accumulated precipitation. This confirms that the errors in the representation of the cut-off strength in Ctrl$_{Bad}$ on 12 October are indeed crucial for the misrepresented HIW. In an additional experiment, the upper-level PV has been modified in a much larger domain covering the entire eastern North Atlantic and the western Mediterranean (30°W–5°E, 25°–65°N; not shown). Compared to Exp$_{PV}$, this led to no further improvement in the PV streamer and precipitation forecast, which confirms the key role of the representation of the cut-off structure for the HIW two days later.

[2]Note that in Figure 7a some fine-scale PV errors remain, because even though the PV inversion algorithm tends to minimize the PV errors by solving a variational minimisation problem, it is not possible to get purely zero PV errors.

TABLE 1 Description of the numerical experiments

Experiment	Forecast base time	Type of modification
$Ctrl_{Good}$	**0000 UTC, 12 October 2016**	—
$Ctrl_{Bad}$	**1800 UTC, 10 October 2016**	—
Exp_{PV}	**1800 UTC, 10 October 2016**	At 0000 UTC, 12 October 2016, the PV in the 30 hr forecast of $Ctrl_{Bad}$ is replaced by the analysis (i.e., the initial state of $Ctrl_{Good}$) in the region around cut-off *Sanchez* (25°–5°W, 35°–55°N, between 100 and 600 hPa).
Exp_{IWVA}	**1800 UTC, 10 October 2016**	At 0000 UTC, 12 October 2016, the specific humidity in the 30 hr forecast of $Ctrl_{Bad}$ is replaced by the analysis (i.e., the initial state of $Ctrl_{Good}$) in the eastern North Atlantic (30°–5°W, 25°–50°N, between 1,010 and 500 hPa).
Exp_{IWVM}	**1800 UTC, 10 October 2016**	At 0000 UTC, 12 October 2016, the specific humidity in the 30 hr forecast of $Ctrl_{Bad}$ is replaced by the analysis (i.e., the initial state of $Ctrl_{Good}$) in the Mediterranean (5°W–20°E, 25°–50°N, between 1,010 and 500 hPa).
$Exp_{PV+IWVA}$	**1800 UTC, 10 October 2016**	Combination of Exp_{PV} and Exp_{IWVA}.

To understand this relationship between the PV errors within the cut-off on 12 October and the misrepresented HIW, we investigate the PV error evolution with the help of Equation (1). We compare $Ctrl_{Bad}$ with Exp_{PV}, such that the different flow evolution in the two runs can be entirely attributed to the PV errors associated with the cut-off at 0000 UTC 12 October. Exp_{PV} and $Ctrl_{Bad}$ are regarded as the reference and forecast evolution, respectively, and PV and wind errors (PV* and v* in Equation (1)) denote departures of the fields in $Ctrl_{Bad}$ from those in Exp_{PV}. To investigate the origin of the positive PV error over southern France (i.e., the eastward shift of the PV streamer in $Ctrl_{Bad}$ with respect to Exp_{PV}) and the processes contributing to its growth, we compute Equation (1) by calculating isentropic two-day backward trajectories starting at 0000 UTC 14 October in the region of the positive PV error on the 320–330 K averaged PV surface. The starting points are highlighted by the red dots in Figure 8b. Following Equation (1), the backward trajectories are computed by advecting the trajectories backwards with the horizontal wind components from the reference flow (i.e., from Exp_{PV}) on each isentrope. Along the backward trajectories, PV*, term 1 and term 2 are traced from the Eulerian datasets, and the PV error tendency $(\Delta PV^*/\Delta t)_{ref}$ and the sum over the non-conservative processes and the residue (NonCons* + Res*) are calculated as described in Section 2.4.

Figure 8a shows the mean evolution of the PV error (grey dashed line), its tendency (black solid line) and the individual terms along the two-day backward trajectories from the positive PV error. At the starting time of the trajectories, at 0000 UTC 14 October, the mean positive PV error (grey dashed, that is, the mean PV error associated with the red dots in Figure 8b) amounts to values larger than 1.5 pvu. This error developed rapidly within the previous 12 hr from slightly negative values at 1200 UTC 13 October to high positive values at the time of the HIW. At earlier times, between 0000 UTC 1200 and 0000 UTC 13 October, the error and its tendency were close to zero. The rapid error growth within the last 12 hr preceding the HIW went along with a strong positive PV error tendency (black line). Apart from the beginning of the error growth, when the sum over the non-conservative term and the residue (green line) was relatively large, the strong positive error tendency can almost entirely be explained by term 1 ($-\mathbf{v}^* \cdot \nabla_\theta PV_{ref}$; dark blue line), that is, the advection of the reference PV field associated with Exp_{PV} by the wind errors. The Eulerian perspective in Figure 8c,d shows that during the peak of this positive PV error tendency, at 1500 UTC 13 October, the air parcels were located on the southeastern side of the PV streamer, which was indeed a region with large positive PV error production via term 1 (Figure 8d). Inspection of the PV and wind error fields at this time (Figure 8c) shows that the error production via term 1 can be explained by the presence of negative PV errors within large parts of the PV streamer and associated anticyclonic wind errors pointing southeastward toward the air parcels at the edge of the streamer. Due to the isentropic PV gradient along the streamer, the wind errors advected high stratospheric PV values associated with Exp_{PV} from the centre of the streamer toward its southeastern part, which resulted in large positive PV error production via term 1 in that region. Thereby, the PV error within the air parcels continuously increased within the

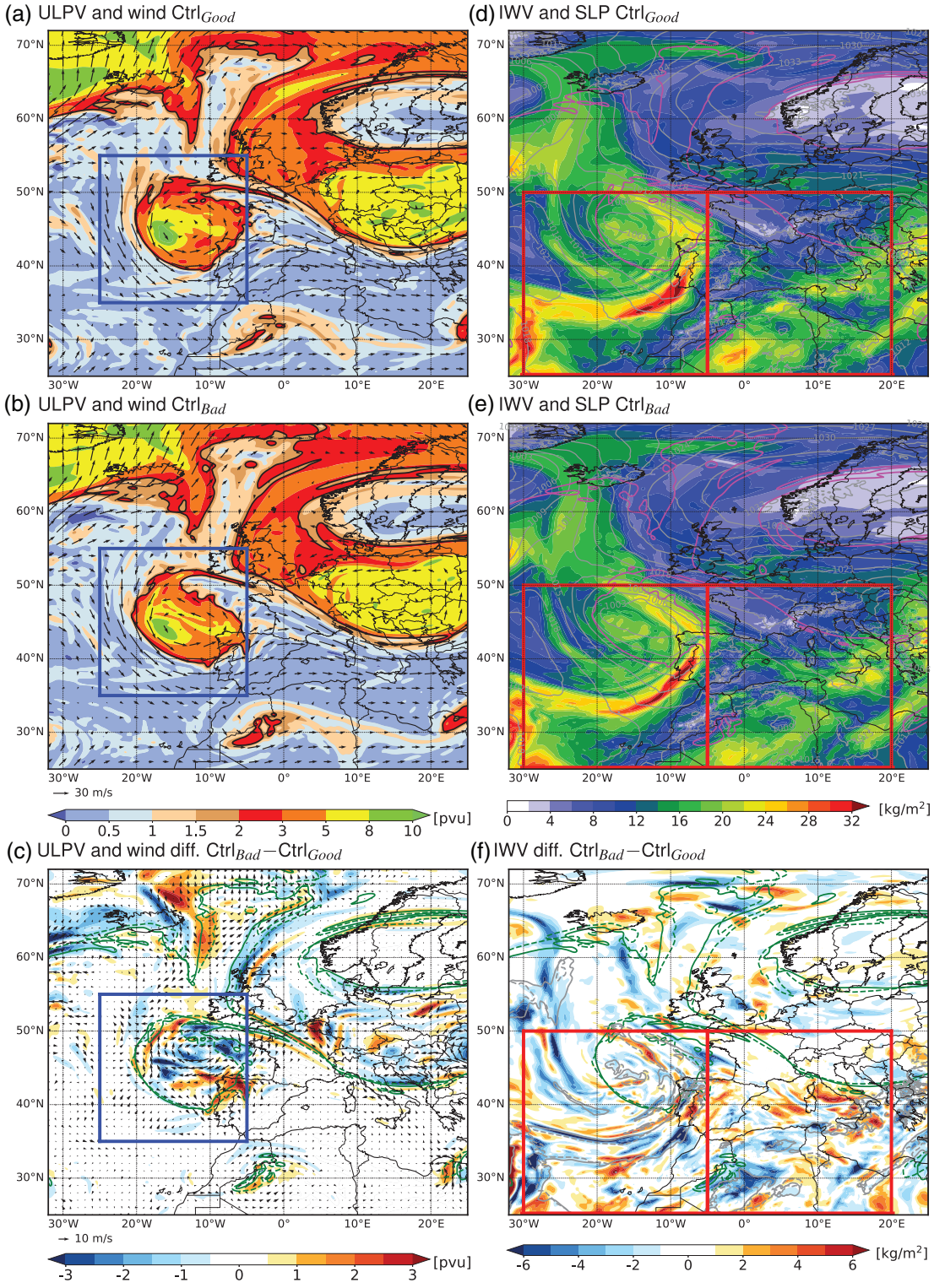

FIGURE 5 Upper-level PV, wind and IWV structure at 0000 UTC 12 October 2016 in the deterministic control forecasts. (a, b) 320–330 K vertically averaged PV (pvu; shading) and wind vectors (m·s^{-1}; arrows) in (a) Ctrl$_{Good}$, and (b) Ctrl$_{Bad}$. (c) Difference in 320–330 K vertically averaged PV (pvu; shading) and wind vectors (m·s^{-1}; arrows) between Ctrl$_{Bad}$ and Ctrl$_{Good}$. The green solid and dashed contours indicate the 2 pvu contour of Ctrl$_{Good}$ and Ctrl$_{Bad}$, respectively. The blue square in (a–c) marks the region where the PV inversion is applied in Exp$_{PV}$. (d, e) 1,010–500 hPa IWV (kg·m^{-2}; shading), sea level pressure (hPa; grey contours every 3 hPa) and 2 pvu contour of 320–330 K vertically averaged PV (magenta) in (d) Ctrl$_{Good}$, and (e) Ctrl$_{Bad}$. (f) Difference in 1,010–500 hPa IWV (kg·m^{-2}; shading) between Ctrl$_{Bad}$ and Ctrl$_{Good}$. The 320–330 K vertically averaged 2 pvu contour (green) and the 20 kg·m^{-2} IWV contour (grey) are shown as solid and dashed lines for Ctrl$_{Good}$ and Ctrl$_{Bad}$, respectively. The red squares in (d–f) mark the region where the moisture is exchanged in Exp$_{IWVA}$ (30°–5°W, 25°–50°N) and Exp$_{IWVM}$ (5°W–20°E, 25°–50°N)

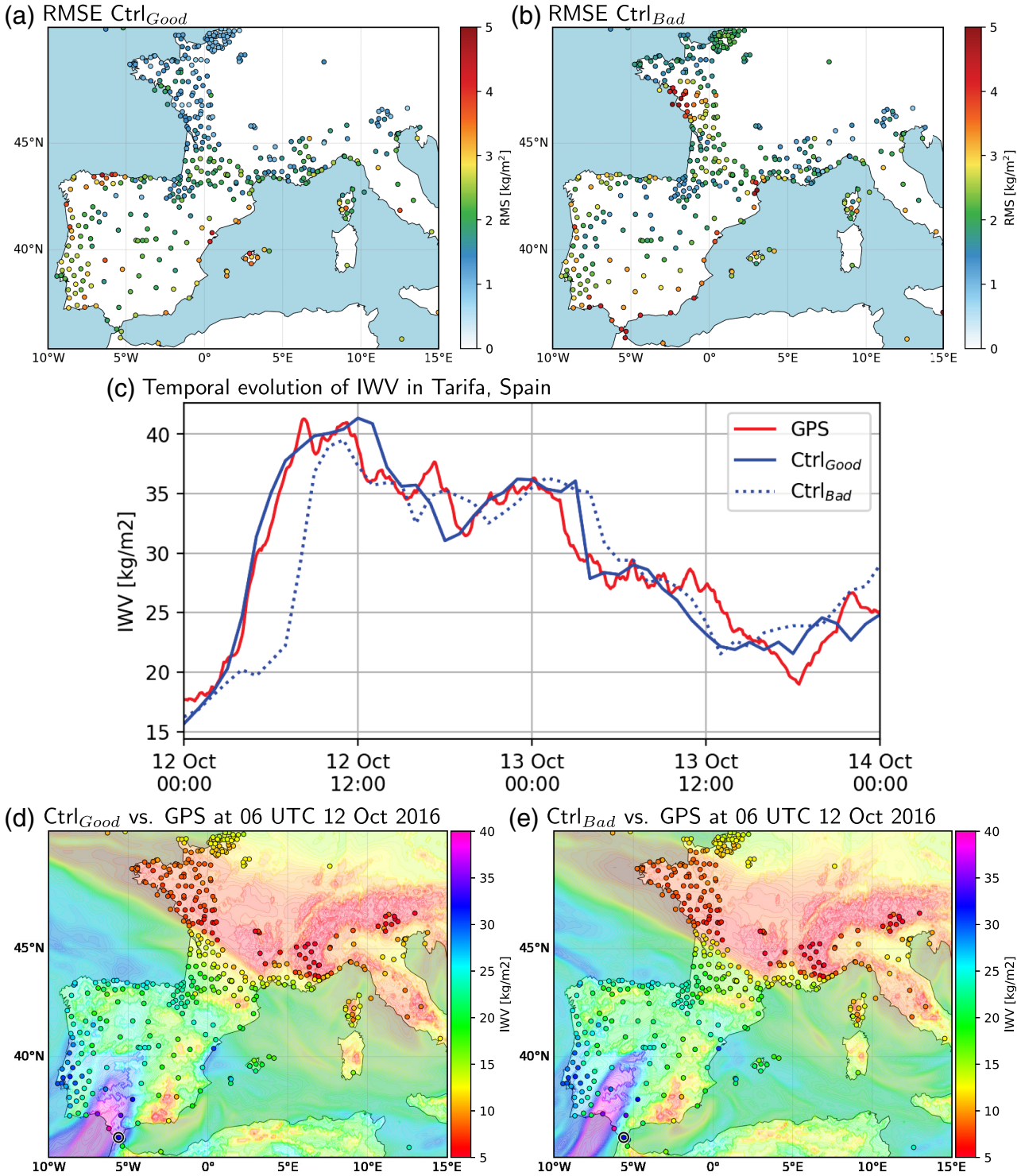

FIGURE 6 Comparison of modelled IWV from $Ctrl_{Good}$ and $Ctrl_{Bad}$ with IWV derived from GPS measurements at different European stations. (a, b) Map showing at each station the RMSE (kg·m^{-2}; coloured dots) of the modelled with respect to the observed hourly values between 0000 UTC 12 October and 0000 UTC 14 October 2016 for (a) $Ctrl_{Good}$ and (b) $Ctrl_{Bad}$. (c) Temporal evolution of the observed (red solid) and the modelled IWV from $Ctrl_{Good}$ (blue solid) and $Ctrl_{Bad}$ (blue dashed), at Tarifa in southern Spain, this station is marked by the black circle in (d, e), which also show observed IWV (kg·m^{-2}; coloured dots) at each station at 0600 UTC 12 October 2016 overlaid on the modelled IWV (colour shading) from (d) $Ctrl_{Good}$ and (e) $Ctrl_{Bad}$ [Colour figure can be viewed at wileyonlinelibrary.com]

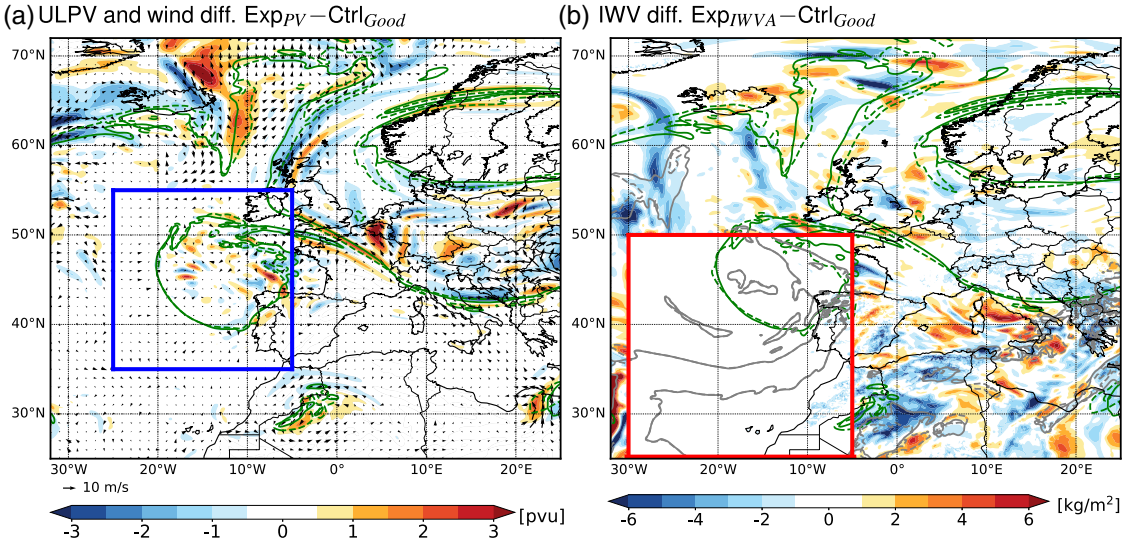

FIGURE 7 (a) is as Figure 5c, but for the difference between Exp_{PV} and $Ctrl_{Good}$, and with the green dashed line showing the 2 pvu contour of Exp_{PV}. The blue square marks the region where the PV inversion is applied in Exp_{PV}. (b) is as Figure 5f, but for the difference between Exp_{IWVA} and $Ctrl_{Good}$, and with the dashed lines showing the 320–330 K vertically averaged 2 pvu contour (green) and the 20 kg·m^{-2} IWV contour (grey) of Exp_{IWVA}. The red square marks the region where the moisture is exchanged in Exp_{IWVA} (30°–5°W, 25°–50°N) [Colour figure can be viewed at wileyonlinelibrary.com]

next hours, while they were advected northward toward southern France.

The origin of the negative PV errors within the streamer which were responsible for the rapid growth of the positive error at its edge can also be investigated with backward trajectories. The air parcels are started at 1500 UTC 13 October from all positions with negative errors within the PV streamer, as illustrated by the purple dots in Figure 9b. In contrast to the positive error, the negative error was already present on 12 October, although it further amplified on 13 October (grey dashed line in Figure 9a). Most air parcels ending up in the northern part of the PV streamer were already located within cut-off *Sanchez* at 0000 UTC 12 October (dark purple dots in Figure 9c) and coinciding with the region of high negative PV errors at that time. Those ending up in the streamer's southern part originated near the UK (light purple), with almost zero initial PV errors. In these air masses, the negative PV error developed about one day later as they merged with the western side of the cut-off (not shown). It formed again mainly via term 1 (compare black and dark blue lines in Figure 9a) from the negative PV errors already present inside the cut-off (not shown).

In summary, this first experiment (Exp_{PV}) and the analysis of the PV error tendency equation reveal that the underestimation of cut-off *Sanchez* in the bad forecast at 0000 UTC 12 October was crucial for the misrepresented HIW event two days later. The negative error was advected downstream and amplified further, and the associated anticyclonic wind errors eventually resulted in positive PV error production at the eastern side of *Sanchez*, which in turn led to an erroneous eastward shift of the streamer and the extreme precipitation over southern France.

4.3 | Forecast sensitivity to the North Atlantic and Mediterranean IWV two days before the event

After revealing the crucial role of the negative PV errors within cut-off *Sanchez* for the HIW two days later, in this part we investigate the sensitivity of the event to the moisture structure in different ocean basins. In the first experiment, Exp_{IWVA}, the specific humidity field in $Ctrl_{Bad}$ is replaced by that of $Ctrl_{Good}$ in the eastern North Atlantic (at 30°–5°W, 25°–50°N, between 1,010 and 500 hPa) two days before the HIW (Figure 7b), without removing the upper-level PV errors (Figure 5c). In the same way, in the second experiment, Exp_{IWVM}, the specific humidity modifications are applied to the Mediterranean and Northern Africa (5°W–20°E, 25°–50°N).

The moisture modifications in the eastern North Atlantic have some impact on the upper-level PV forecast, with a slight decrease of the positive error over southern France compared to $Ctrl_{Bad}$, but also considerably weaker negative errors over Spain (Figure 4c). In terms of precipitation, the modifications lead to a marked improvement in the forecast, particularly obvious over the Mediterranean Sea (Figure 4h). However, the sensitivity of the forecasts to the North Atlantic IWV on 12 October is

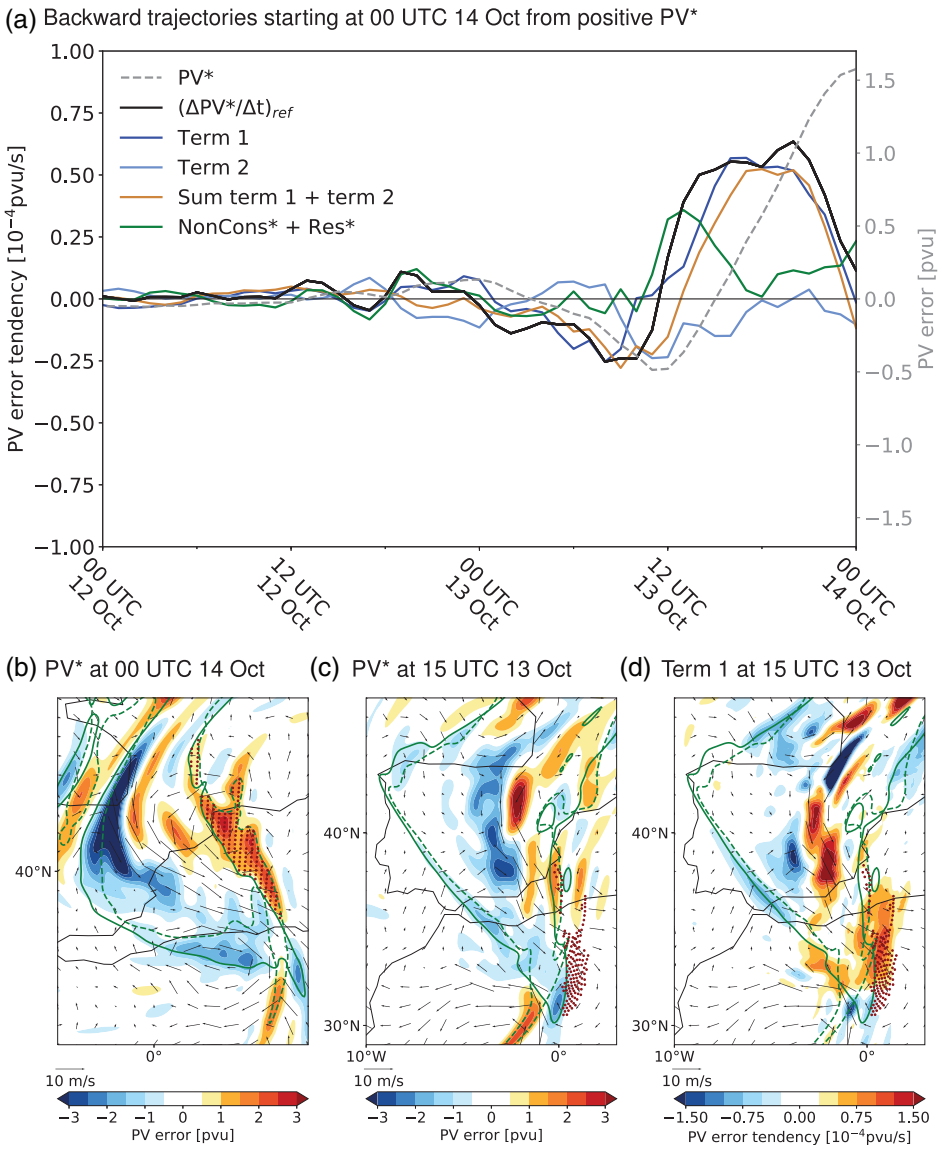

FIGURE 8 (a) Temporal evolution of individual contributions (coloured lines) to the PV error growth of $Ctrl_{Bad}$ with respect to Exp_{PV} ($Ctrl_{Bad}$ minus Exp_{PV}) along backward trajectories starting at 0000 UTC 14 October 2016 from the positive PV errors at the eastern edge of PV streamer *Sanchez* (red dots in (b) show the starting positions). (b) PV errors (pvu; shading) and wind vector errors ($m \cdot s^{-1}$; arrows) in $Ctrl_{Bad}$ at 0000 UTC 14 October 2016, together with the 2 pvu contour in Exp_{PV} (green solid) and $Ctrl_{Bad}$ (green dashed). Overlaid are the starting positions of the backward trajectories from the positive PV error (red dots). (c) is a as (b), but at 1500 UTC 13 October 2016, and with the red dots showing the position of backward trajectories from the positive PV error at that time step. (d) Term 1 of Equation (1) (10^{-4} pvu$\cdot s^{-1}$; shading), at 1500 UTC 13 October 2016. The other fields are as in (c). The individual contributions to the PV error growth and all Eulerian fields are shown for 320–330 K vertically averaged PV

much smaller than the sensitivity to the cut-off structure (compare Figures 4c,h and b,g). The moisture modifications in the Mediterranean have almost no impact on the upper-level PV forecast (Figure 4d). They lead to a slight improvement of the precipitation forecast (Figure 4i), but, surprisingly, the improvement is much smaller than when applying the modifications to the North Atlantic moisture. An additional experiment has been conducted where the moisture has been modified both in the eastern North Atlantic and the Mediterranean at the same time (not shown), which led to almost exactly the same response in terms of upper-level PV and precipitation as in Figure 4c,h for the experiment with good IWV in the North Atlantic only. This confirms that the HIW forecast shows some sensitivity to the North Atlantic moisture structure, but only relatively weak sensitivity to the moisture in the Mediterranean. Note that this does not imply that the precipitation over southern France was entirely fed by moisture originating in the North Atlantic. Most likely, local Mediterranean moisture sources also contributed to the HIW, but the results show that their detailed representation in the simulations only had a small impact on the forecast quality.

In order to understand the sensitivity of the forecasts to the North Atlantic humidity structure two days earlier, we compare Exp_{IWVA} with $Ctrl_{Bad}$. Consistent with Figure 4a,c, the difference in upper-level PV between $Ctrl_{Bad}$ and Exp_{IWVA} at the time of the HIW event confirms that the eastern edge of the PV streamer is located slightly further to the east in $Ctrl_{Bad}$ than in Exp_{IWVA}, that is, there is a small positive upper-level PV error in $Ctrl_{Bad}$ with respect to Exp_{IWVA} (Figure 10a). This difference between the two runs can be followed back in time until 1700 UTC 13 October (see area between the Iberian Peninsula and the Balearic Islands highlighted by the green square in Figure 10b). In that region, WCB intersections

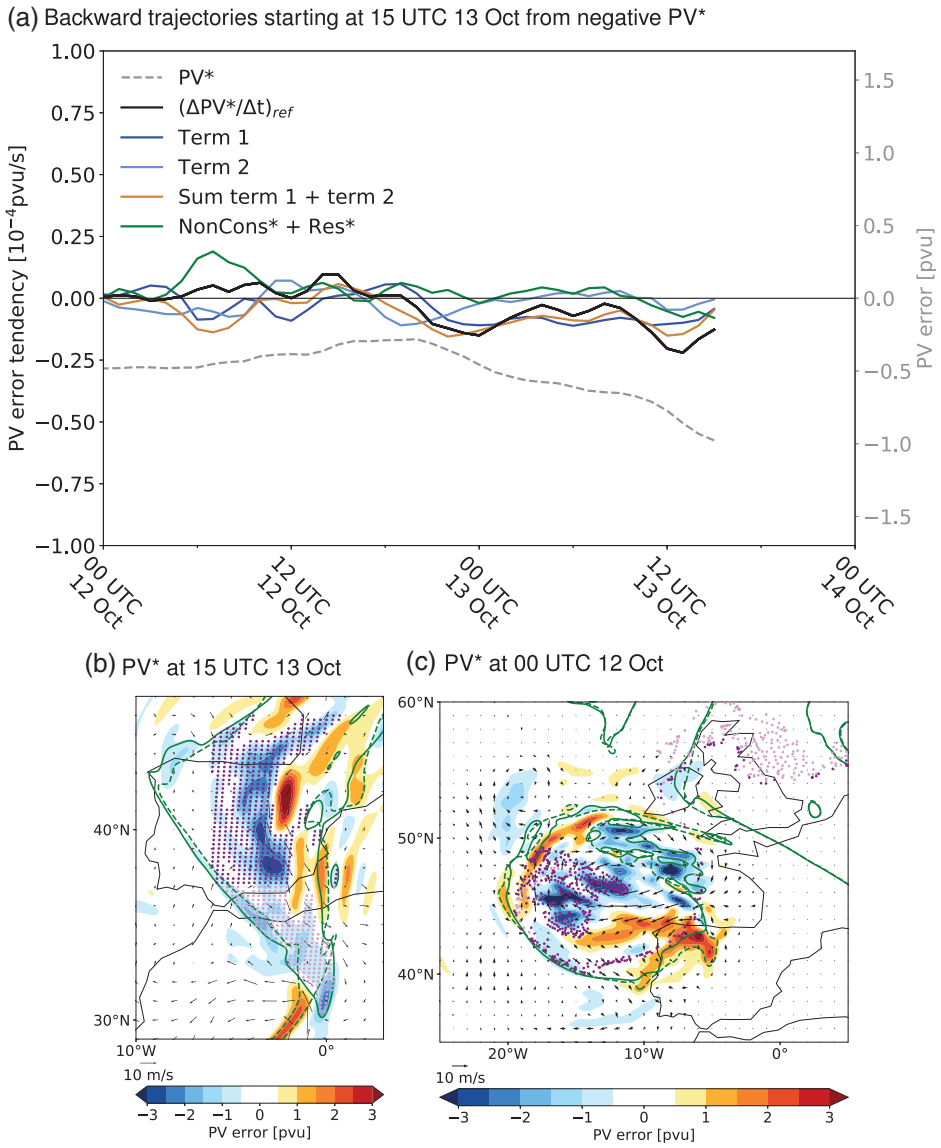

FIGURE 9 (a) As Figure 8a, but for backward trajectories starting at 1500 UTC 13 October 2016 from the domain with negative PV errors within the PV streamer (purple dots in (b) mark the starting positions). (b, c) are as Figure 8b but at (b) 1500 UTC 13 October and (c) 0000 UTC 12 October, together with the position of the backward trajectories from the negative PV error (light/dark purple dots for starting positions south/north of 37°N at 1500 UTC 13 October)

with the 325 K isentrope (black dots in Figure 10c,d) indicate the presence of WCB air parcels in the upper troposphere in both experiments. As described in the introduction, intense cloud-diabatic processes along the ascending WCBs generate negative PV anomalies in the WCB outflow, which can erode upper-level troughs and amplify ridges. Hence, the black dots in Figure 10c,d illustrate the impact of the low-PV air in the WCB outflow on the tropopause structure. Comparison of the two simulations shows a much larger number of WCB intersections in $\mathrm{Exp_{IWVA}}$ (Figure 10d) than in $\mathrm{Ctrl_{Bad}}$ (Figure 10c). This implies stronger diabatic erosion of the streamer's leading edge by the stronger WCB outflow in $\mathrm{Exp_{IWVA}}$ and accordingly a westward displacement compared to $\mathrm{Ctrl_{Bad}}$. In addition, the indirect effect of stronger diabatic heating is to create stronger divergent outflow at upper levels, which pushes the negative PV outward and amplifies the ridge ahead of the PV streamer (Riemer *et al.*, 2008; Archambault *et al.*, 2013). Indeed, we checked that ahead of the PV streamer the negative PV advection by the divergent winds is stronger in $\mathrm{Exp_{IWVA}}$ than in $\mathrm{Ctrl_{Bad}}$ (not shown). Thus, the slight westward shift of the leading edge of the PV streamer in $\mathrm{Exp_{IWVA}}$ is due to a combination of both the direct injection of more low-PV air into the tropopause region and the indirect effect associated with the stronger divergent outflow.

The stronger WCB activity in $\mathrm{Exp_{IWVA}}$ can be understood when following the air parcels ending up in the green square back in time until 0000 UTC 12 October (Figure 10c,d). The path of the trajectories is very similar in the two runs. They originate in the eastern North Atlantic, with one inflow region west of Portugal around 22°W/40°N, and a second one west of Morocco around 15°W/34°N. Comparison with Figure 5d–f shows that these inflow regions correspond to the two filaments with high IWV, which are too narrow in $\mathrm{Ctrl_{Bad}}$ and where the

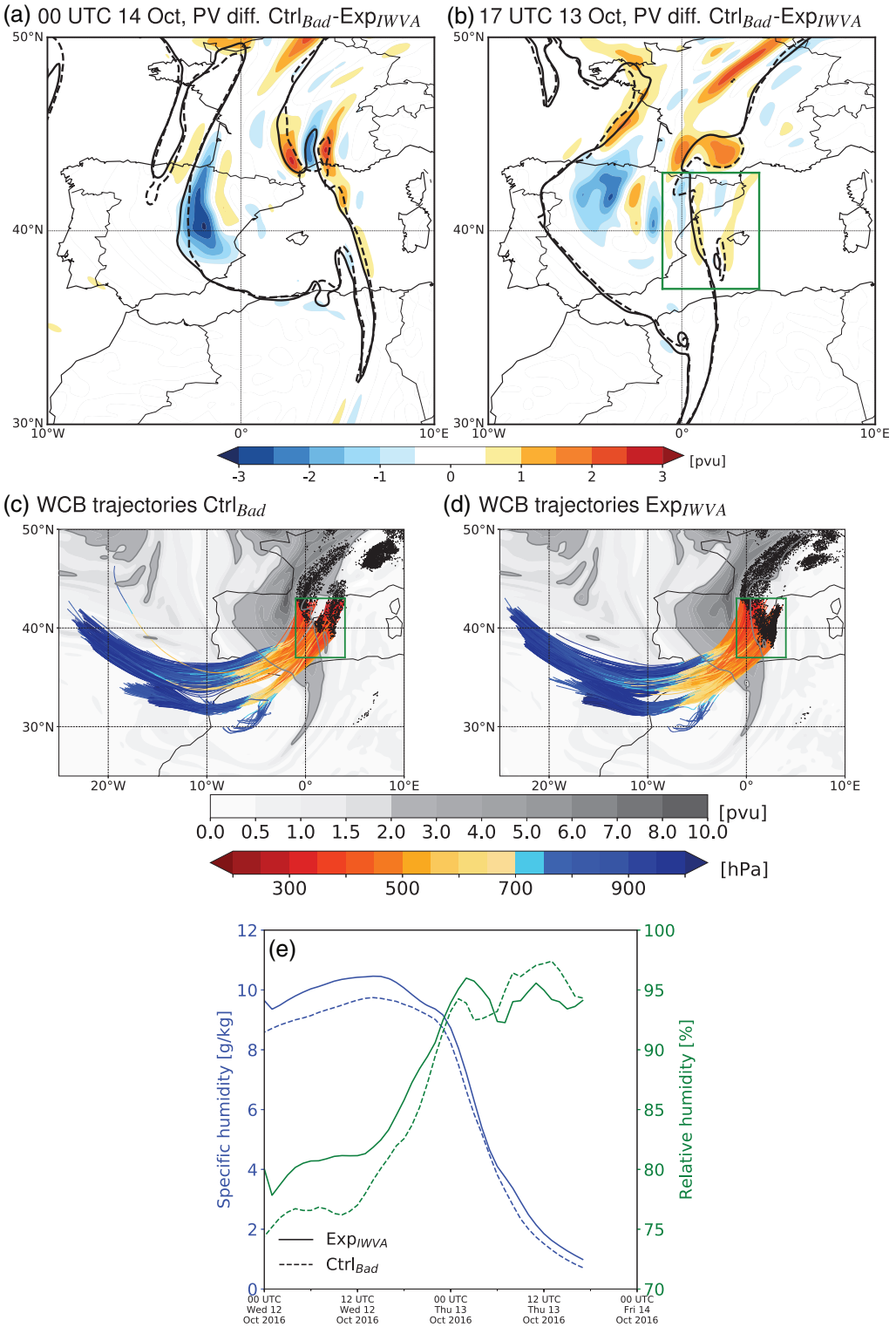

FIGURE 10 (a, b) 320–330 K vertically averaged PV error in $Ctrl_{Bad}$ with respect to Exp_{IWVA} ($Ctrl_{Bad}$ minus Exp_{IWVA}) at (a) 0000 UTC 14 October and (b) 1700 UTC 13 October 2016, together with the 2 pvu contour in Exp_{IWVA} (black solid) and $Ctrl_{Bad}$ (black dashed). (c, d) Upper-level PV (pvu; grey shading) and WCB intersections with 325 ± 10 K at 1700 UTC 13 October (black dots) in (c) $Ctrl_{Bad}$ and (d) Exp_{IWVA}. Overlaid are WCB trajectories (coloured by pressure; hPa) starting at 0000 UTC 12 October and intersecting the 325 ± 10 K isentrope at 1700 UTC 13 October in the region highlighted by the green square. The WCB trajectories are shown only between their starting time at 0000 UTC 12 October and the time they intersect the 325 K isentrope at 1700 UTC 13 October; the continuation of their two-day ascent during the following 7 hr is omitted. (e) Temporal evolution of the mean specific ($g \cdot kg^{-1}$; blue) and relative (%, green) humidity along the WCB trajectories shown in (c) for $Ctrl_{Bad}$ (dashed) and in (d) for Exp_{IWVA} (solid)

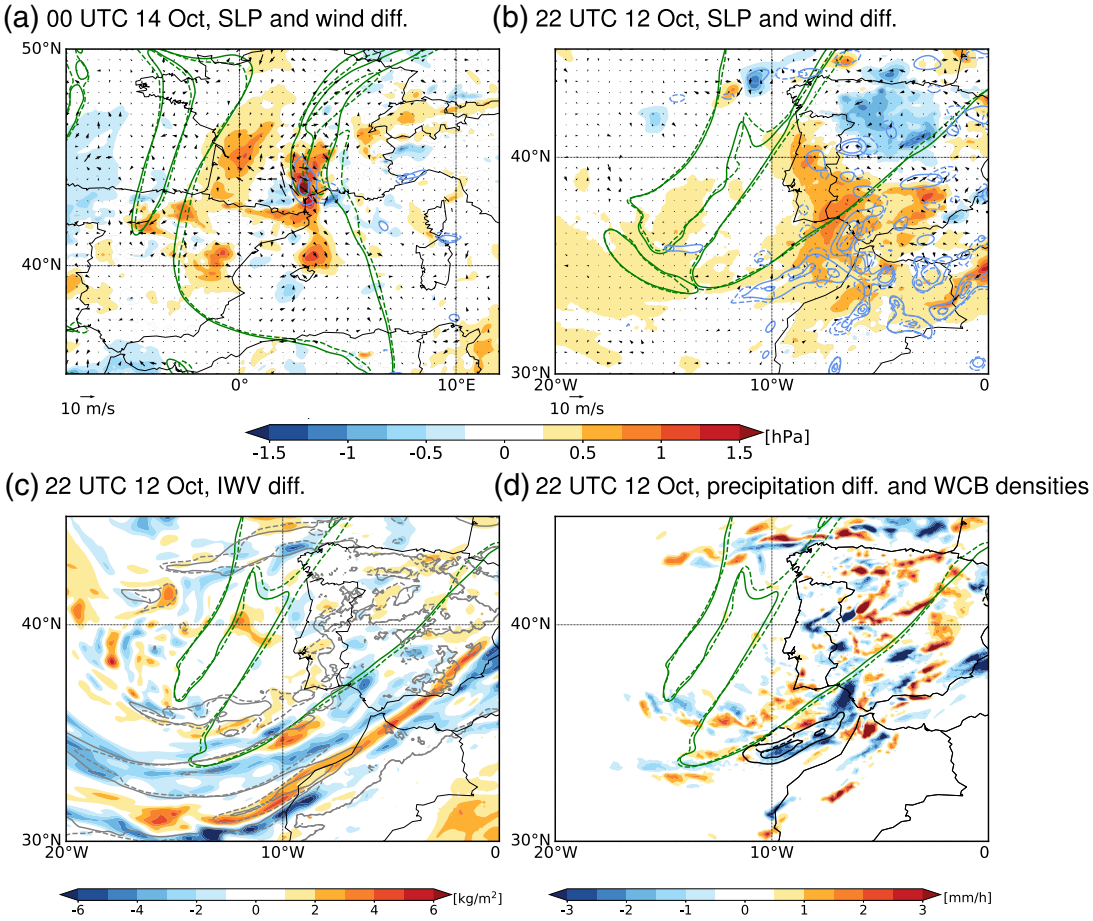

FIGURE 11 (a, b) Sea level pressure error (hPa; shading) and horizontal wind error at 850 hPa in $Ctrl_{Bad}$ with respect to Exp_{IWVA} ($Ctrl_{Bad}$ minus Exp_{IWVA}) at (a) 0000 UTC 14 October and (b) 2200 UTC 12 October 2016. The green contours show the 320–330 K vertically averaged 2 pvu isoline and the blue contours the upward vertical motions at 700 hPa at −2 and −4 $Pa \cdot s^{-1}$ (solid for Exp_{IWVA} and dashed for $Ctrl_{Bad}$). (c) 1,010–500 hPa IWV error ($kg \cdot m^{-2}$; shading) and (d) hourly accumulation precipitation error ($mm \cdot hr^{-1}$; shading) in $Ctrl_{Bad}$ with respect to Exp_{IWVA} at 2200 UTC 12 October. In (c) the 20 $kg \cdot m^{-2}$ IWV contour is overlaid in grey, and in (d) the densities of ascending WCB air parcels located between 800 and 400 hPa (black contours for 0.02 and 0.04 WCB air parcels km^{-2}), with solid contours for Exp_{IWVA} and dashed contours for $Ctrl_{Bad}$. The green contours in (c, d) are as in (b) [Colour figure can be viewed at wileyonlinelibrary.com]

values are underestimated (also Figure 6d,e). The mean temporal evolution of humidity along the trajectories confirms that the values in the WCB inflow are indeed lower in $Ctrl_{Bad}$ in the first 24 hr (on average about 1 $g \cdot kg^{-1}$ lower specific humidity and 5% lower relative humidity; Figure 10e), as the trajectories move into the Mediterranean along the too narrow high-humidity band. This indicates that the reduced WCB activity in $Ctrl_{Bad}$ compared to Exp_{IWVA} which is responsible for the weaker diabatic erosion of the streamer's leading edge can be explained by the underestimation of the initial humidity in the WCB inflow region.

The slight improvement in the representation of the upper-level PV structure in Exp_{IWVA} compared to $Ctrl_{Bad}$ (Figures 10a and 4c) potentially also contributes to the improvement in the precipitation structure (Figure 4h). However, most of the precipitation improvement can be explained by a direct impact of the humidity in the WCB inflow on the low-level circulation. At the time of the HIW event, $Ctrl_{Bad}$ is associated with a positive sea level pressure anomaly of about 1.5 hPa and an anticyclonic low-level wind anomaly with respect to Exp_{IWVA} in the department of Hérault over southern France (Figure 11a). The anticyclonic wind anomaly in $Ctrl_{Bad}$ impedes the northeastward transport of the warm and moist air masses from the Mediterranean towards that region and shifts the low-level convergence line eastward, which goes along with an eastward shift of the region of ascent and precipitation formation (dashed and solid blue contours in Figure 11a for the ascent regions in $Ctrl_{Bad}$ and Exp_{IWVA}, respectively). The positive sea level pressure anomaly had been advected from the eastern North Atlantic toward southern France during the previous day (Figure 11b). At 2200 UTC 12 October, it coincided with a region of

reduced IWV (Figure 11c), WCB ascent and precipitation (Figure 11d) at the leading side of the PV streamer. Atmospheric warming by latent heat release during cloud formation and mass loss during precipitation both lead to a decrease in the surface pressure (e.g., the surface pressure tendency equation described by Fink *et al.*, 2012). The lower IWV and accordingly the weaker diabatic heating and precipitation formation in $Ctrl_{Bad}$ resulted in a weaker surface pressure decrease, which explains the positive pressure anomaly with respect to Exp_{IWVA}.

To sum up, the slight improvement of the HIW forecasts when removing the humidity errors in the eastern North Atlantic two days before the event is caused by an increase in the humidity in the WCB inflow region (mainly through a broadening of the high-humidity band) and associated stronger WCB ascent and diabatic heating. At low levels the stronger WCB activity led to stronger surface pressure decrease and cyclonic circulation at the leading edge of the streamer. This anomaly with respect to $Ctrl_{Bad}$ was continuously advected northeastward from the eastern North Atlantic toward the Gulf of Lion, where its northern part eventually created an easterly wind and hence a westward displacement of the precipitation compared to $Ctrl_{Bad}$. At the same time, at upper levels the stronger WCB ascent and diabatic heating resulted in stronger diabatic erosion of the PV streamer's leading edge and hence a westward displacement of the upper-level disturbance.

4.4 | Forecast sensitivity to the upper-level PV and North Atlantic IWV two days before the event

In the previous experiments we saw that the HIW forecasts are highly sensitive to the representation of the upper-level PV within cut-off *Sanchez* two days earlier and, to a smaller extent, also to the representation of the moisture structure in the eastern North Atlantic. In this final experiment, $Exp_{PV+IWVA}$, we assess the combined effect of Exp_{PV} and Exp_{IWVA} on the HIW forecast, that is, on 12 October we replace at the same time the upper-level PV in the region around cut-off *Sanchez* and the specific humidity in the eastern North Atlantic of $Ctrl_{Bad}$ by the fields of $Ctrl_{Good}$ (Figure 7a,b). As shown in Figure 4e,j, in the region of the HIW over southern France the combination of the good upstream upper-level PV and IWV leads to the strongest forecast improvement of all experiments. Compared to Exp_{PV}, the upper-level PV error over southern France has further decreased (compare Figure 4e and b), and the precipitation error has almost entirely disappeared (Figure 4j). The combined effect of the good cut-off structure and the good North Atlantic IWV is even more pronounced than the sum of the effects from the two separate experiments. This can be explained by an interaction between the dry and moist dynamics: the deeper cut-off associated with the good run triggered even stronger WCB ascent than the good North Atlantic IWV structure alone, which went along with stronger low-level cyclonic circulation and upper-level diabatic PV erosion, and hence a further improvement of the HIW forecasts.

5 | SUMMARY AND CONCLUSIONS

Despite significant advances in numerical weather prediction during recent decades, the prediction of high-impact weather events like heavy precipitation, flash floods and strong winds continues to be challenging. In this study, we evaluated the representation of an extreme precipitation event over southern France in probabilistic and deterministic forecasts from the Météo-France global operational model ARPEGE, and quantified the sensitivity of the HIW forecast to the upstream upper-level flow and the low-level moisture structure in the Mediterranean and eastern North Atlantic two days earlier. The event occurred in October 2016 during the international field experiment NAWDEX (Schäfler *et al.*, 2018). The eastward propagation of an upper-level PV streamer, referred to as *Sanchez*, induced strong moisture advection from the Mediterranean toward southern France, resulting in heavy precipitation and strong winds. We verified the forecast performance of a ten-member ensemble with lead times between 48 and 168 hr and two deterministic forecasts with lead times of 48 and 78 hr, and used PV inversion and moisture replacement methods to assess how specific changes in the PV and moisture structure a few days prior to the event affected the forecast quality. To quantify the evolution of upper-level PV errors, a novel approach was used based on the computation of the PV error tendency equation of Davies and Didone (2013) with isentropic backward trajectories from the error field.

Many of the 48–168 hr ensemble forecasts and the 78 hr deterministic forecast predicted the maximum of the extreme precipitation and the location of the upper-level PV streamer too far to the east and, depending on their lead time, they overestimated (48–96 hr forecasts) or underestimated (102–168 hr forecasts) the precipitation intensity. In general, the forecast quality decreased with increasing lead time. Comparison of the poor deterministic 78 hr forecast with a fairly good 48 hr forecast showed that the eastward shift of the predicted HIW primarily resulted from an underestimation of the intensity of PV cut-off *Sanchez* – the precursor to PV streamer *Sanchez* – two days prior to the HIW, and the downstream propagation and growth of these errors in the vicinity of *Sanchez*.

A correction of the upper-level PV structure two days before the event within cut-off *Sanchez* led to a substantial improvement of the HIW forecast.

In addition to the PV cut-off as the main error source, errors in the moisture structure in the eastern North Atlantic also contributed to the eastward shift of the HIW two days later, although to a much smaller extent. Specifically, an underestimation of the Atlantic moisture in the WCB inflow region two days before the event, mainly characterised by a too narrow filament with high humidity south of the cut-off, resulted in an underestimation of the WCB ascent and diabatic heating, which went along with too weak diabatic erosion of PV streamer *Sanchez* and a slight eastward shift of its leading edge. This confirms the findings from Schäfler *et al.* (2011) and Schäfler and Harnisch (2015) that inaccuracies in the representation of the low-level moisture can play an important role in the evolution of the WCB and the upper-level flow. At the same time, the underestimation of the moisture in the WCB inflow in the eastern North Atlantic affected the low-level circulation by producing weak anticyclonic pressure and wind anomalies which were advected into the Mediterranean, where they contributed to the eastward shift of the precipitation maximum. The forecast quality of the HIW event could be significantly improved when correcting at the same time the upper-level PV structure associated with cut-off *Sanchez* and the moisture structure in the WCB inflow region in the eastern North Atlantic two days before the event. This is in line with the findings from earlier studies that remote Atlantic moisture sources can be crucial for Mediterranean extreme precipitation (e.g., Turato *et al.*, 2004; Winschall *et al.*, 2012; Duffourg and Ducrocq, 2013). In contrast, corrections of the moisture in the Mediterranean, where the values were mostly overestimated, had much less impact on the HIW forecast. This does not imply that all the moisture precipitating over southern France must have originated over the North Atlantic and none over the Mediterranean; on the contrary, it is very likely that the precipitation event was also fed by local Mediterranean moisture sources. However, interestingly the detailed representation of the Mediterranean moisture in the model only had a small effect on the quality of the forecast.

The corrections of the PV field within cut-off *Sanchez* and the moisture in the eastern North Atlantic significantly improved the HIW forecast, especially in terms of location. However, some errors remained, both in the representation of the PV streamer and the precipitation pattern. When applying the corrections to a larger domain, this did not lead to a further improvement of the forecasts, suggesting that other processes must have been responsible for the remaining errors. Possible error sources are small-scale processes like convection, microphysics and turbulence, and their complex and nonlinear interactions with larger scales. Such convective-scale processes, which have been parametrized in the present study, have been shown to be highly relevant for Mediterranean HIW (e.g., Ducrocq *et al.*, 2008), and associated errors can grow rapidly and thereby affect the forecast quality on the meso- and synoptic scales (e.g., Zhang *et al.*, 2007; Selz and Craig, 2015). In particular, such small-scale processes also might have an effect on the amplitude and structure of the precipitation, which have not been investigated in detail in the present study. A convection-permitting model would be more appropriate to tackle this problem. Indeed, short-range precipitation forecasts of the convection-permitting AROME-EPS (driven by global ARPEGE fields) capture the rainfall accurately in terms of intensity and location (Keil *et al.*, 2020).

The findings of this study show that the prediction of the exact location and intensity of high-impact weather over Europe is still challenging. Downstream error propagation and moist dynamics can have an important impact on forecast quality. The importance of moist dynamics confirms one of the overarching hypotheses of the NAWDEX field campaign that diabatic processes can play an important role for the prediction of severe weather over Europe (Schäfler *et al.*, 2018). Furthermore, our study demonstrates that targeted changes in the upper-level PV and low-level moisture fields prior to the event can significantly improve the quality of the forecasts. One way to improve the low-level moisture field would be to add more humidity observations over the ocean in the data assimilation system. In addition, once the analysis is obtained, if there are obvious discrepancies between the analysis and observational data such as water vapour and ozone satellite imagery, PV modifications can be made by hand to get a new initial state that fits better with the observations, as proposed by Arbogast *et al.* (2012).

Our study focused on the impact of existing upper- and low-level errors on the forecast quality of the HIW a few days later, not on the origin of these errors. A brief analysis of the negative PV errors within cut-off *Sanchez*, which were a persistent pattern among many ensemble members, showed that they typically developed a few hours after forecast initialisation, most likely due to a combination of errors in the representation of latent heating and radiative cooling. In a future study, the origin of the underestimated PV values and the role of diabatic processes could be investigated in more detail with NAWDEX observations obtained from cut-off *Sanchez* about four days prior to the HIW. More generally, it would also be interesting to investigate whether the ARPEGE model systematically underestimates the intensity of cut-offs and, if so, whether this

goes along with location errors in the forecast precipitation downstream.

AUTHOR CONTRIBUTIONS

Hanin Binder: conceptualization; formalAnalysis; fundingAcquisition; methodology; Software; writingOriginalDraft. **Gwendal Rivière:** conceptualization; formalAnalysis; fundingAcquisition; methodology; writingReviewEditing. **Philippe Arbogast:** conceptualization; methodology; writingReviewEditing. **Karine Maynard:** conceptualization; investigation; methodology; writingReviewEditing. **Pierre Bosser:** formalAnalysis; methodology; writingReviewEditing. **Bruno Joly:** methodology; writingReviewEditing. **Carole Labadie:** methodology; writingReviewEditing.

ACKNOWLEDGEMENTS

H.B. acknowledges funding from the Swiss National Science Foundation (SNSF) via grants 175161 and 185049, and from the French National Research Agency (ANR) via the project DIP-NAWDEX (grant: ANR-17-CE01-0010). We are grateful to Michael Sprenger (ETH Zurich) for his technical support with the installation of LAGRANTO and the SAL method in the ARPEGE model, and to Heini Wernli (ETH Zurich) and two anonymous reviewers for valuable comments and discussions.

ORCID

Hanin Binder https://orcid.org/0000-0003-3001-1344
Gwendal Rivière https://orcid.org/0000-0002-6056-5973

REFERENCES

Arbogast, P., Maynard, K. and Crepin, F. (2008) Ertel potential vorticity inversion using a digital filter initialization method. *Quarterly Journal of the Royal Meteorological Society*, 134, 1287–1296.

Arbogast, P., Maynard, K. and Piriou, C. (2012) About the reliability of manual model PV corrections to improve forecasts. *Weather and Forecasting*, 27, 1554–1567.

Archambault, H.M., Bosart, L.F., Keyser, D. and Cordeira, J.M. (2013) A climatological analysis of the extratropical flow response to recurving western North Pacific tropical cyclones. *Monthly Weather Review*, 141, 2325–2346.

Argence, S., Lambert, D., Richard, E., Chaboureau, J.P., Arbogast, J.P. and Maynard, K. (2009) Improving the numerical prediction of a cyclone in the Mediterranean by local potential vorticity modifications. *Quarterly Journal of the Royal Meteorological Society*, 135, 865–879.

Bauer, P., Thorpe, A. and Brunet, G. (2015) The quiet revolution of numerical weather prediction. *Nature*, 525, 47–55.

Baumgart, M., Riemer, M., Wirth, V., Teubler, F. and Lang, S.T. (2018) Potential vorticity dynamics of forecast errors: a quantitative case study. *Monthly Weather Review*, 146, 1405–1425.

Bechtold, P., Bazile, E., Guichard, F., Mascart, P. and Richard, E. (2001) A mass-flux convection scheme for regional and global models. *Quarterly Journal of the Royal Meteorological Society*, 127, 869–886.

Binder, H., Boettcher, M., Joos, H. and Wernli, H. (2016) The role of warm conveyor belts for the intensification of extratropical cyclones in Northern Hemisphere winter. *Journal of the Atmospheric Sciences*, 73, 3997–4020.

Bock, O., Bosser, P., Pacione, R., Nuret, M., Fourrié, N. and Parracho, A. (2016) A high-quality reprocessed ground-based GPS dataset for atmospheric process studies, radiosonde and model evaluation, and reanalysis of HyMeX Special Observing Period. *Quarterly Journal of the Royal Meteorological Society*, 142, 56–71.

Boisserie, M., Decharme, B., Descamps, L. and Arbogast, P. (2016a) Land surface initialization strategy for a global reforecast dataset. *Quarterly Journal of the Royal Meteorological Society*, 142, 880–888.

Boisserie, M., Descamps, L. and Arbogast, P. (2016b) Calibrated forecasts of extreme windstorms using the Extreme Forecast Index (EFI) and Shift of Tails (SOT). *Weather and Forecasting*, 31, 1573–1589.

Bosser, P. and Bock, O. (2021) IWV retrieval from ground GNSS receivers during NAWDEX. *Advances in Geosciences*, 55, 13–22.

Bougeault, P. (1985) A simple parameterization of the large-scale effects of cumulus convection. *Monthly Weather Review*, 113, 2108–2121.

Browning, K.A. (1990). Organization of clouds and precipitation in extratropical cyclones, pp. 129–153 in Extratropical Cyclones: The Erik Palmén Memorial Volume, Newton, C.W., Holopainen, E.O. (eds). Boston, MA: American Meteorological Society.

Courtier, P., Freydier, C., Geleyn, J.-F., Rabier, F. and Rochas, M. (1991). The Arpege project at Météo-France, pp. 193–231 in Proceedings of Seminar on Numerical Methods in Atmospheric Models, 9–13 September 1991. Reading, UK: ECMWF.

Davies, H.C. and Didone, M. (2013) Diagnosis and dynamics of forecast error growth. *Monthly Weather Review*, 141, 2483–2501.

Davis, C., Brown, B. and Bullock, R. (2006) Object-based verification of precipitation forecasts. Part I: methodology and application to mesoscale rain areas. *Monthly Weather Review*, 134, 1772–1784.

Dee, D.P., Uppala, S.M., Simmons, A.J., Berrisford, P., Poli, P., Kobayashi, S., Andrae, U., Balmaseda, M.A., Balsamo, G., Bauer, P., Bechtold, P., Beljaars, A.C.M., van de Berg, L., Bidlot, J., Bormann, N., Delsol, C., Dragani, R., Fuentes, M., Geer, A.J., Haimberger, L., Healy, S.B., Hersbach, H., Hólm, E.V., Isaksen, L., Kållberg, P., Köhler, M., Matricardi, M., McNally, A.P., Monge-Sanz, B.M., Morcrette, J.-J., Park, B.-K., Peubey, C., de Rosnay, P., Tavolato, C., Thépaut, J.-N. and Vitart, F. (2011) The ERA-Interim reanalysis: configuration and performance of the data assimilation system. *Quarterly Journal of the Royal Meteorological Society*, 137, 553–597.

Descamps, L., Labadie, C., Joly, A., Bazile, E., Arbogast, P. and Cébron, P. (2015) PEARP, the Météo-France short-range ensemble prediction system. *Quarterly Journal of the Royal Meteorological Society*, 141, 1671–1685.

Doyle, J.D., Amerault, C., Reynolds, C.A. and Reinecke, P.A. (2014) Initial condition sensitivity and predictability of a severe extratropical cyclone using a moist adjoint. *Monthly Weather Review*, 142, 320–342.

Ducrocq, V., Ricard, D., Lafore, J.-P. and Orain, F. (2002) Storm-scale numerical rainfall prediction for five precipitating events over

France: on the importance of the initial humidity field. *Weather and Forecasting*, 17, 1236–1256.

Ducrocq, V., Nuissier, O., Ricard, D., Lebeaupin, C. and Thouvenin, T. (2008) A numerical study of three catastrophic precipitating events over southern France. II: mesoscale triggering and stationarity factors. *Quarterly Journal of the Royal Meteorological Society*, 134, 131–145.

Ducrocq, V., Braud, I., Davolio, S., Ferretti, R., Flamant, C., Jansa, A., Kalthoff, N., Richard, E., Taupier-Letage, I., Ayral, P.-A., Belamari, S., Berne, A., Borga, M., Boudevillain, B., Bock, O., Boichard, J.-L., Bouin, M.-N., Bousquet, O., Bouvier, C., Chiggiato, J., Cimini, D., Corsmeier, U., Coppola, L., Cocquerez, P., Defer, E., Delanoë, J., Girolamo, P.D., Doerenbecher, A., Drobinski, P., Dufournet, Y., Fourrié, N., Gourley, J.J., Labatut, L., Lambert, D., Coz, J.L., Marzano, F.S., Molinié, G., Montani, A., Nord, G., Nuret, M., Ramage, K., Rison, W., Roussot, O., Said, F., Schwarzenboeck, A., Testor, P., Van-Baelen, J., Vincendon, B., Aran, M. and Tamayo, J. (2014) HyMeX-SOP1: the field campaign dedicated to heavy precipitation and flash flooding in the northwestern Mediterranean. *Bulletin of the American Meteorological Society*, 95, 1083–1100.

Duffourg, F. and Ducrocq, V. (2011) Origin of the moisture feeding the heavy precipitating systems over southeastern France. *Natural Hazards and Earth System Sciences*, 11, 1163.

Duffourg, F. and Ducrocq, V. (2013) Assessment of the water supply to Mediterranean heavy precipitation: a method based on finely designed water budgets. *Atmospheric Science Letters*, 14, 133–138.

Fehlmann, R. and Quadri, C. (2000) Predictability issues of heavy Alpine south-side precipitation. *Meteorology and Atmospheric Physics*, 72, 223–231.

Fink, A.H., Pohle, S., Pinto, J.G. and Knippertz, P. (2012) Diagnosing the influence of diabatic processes on the explosive deepening of extratropical cyclones. *Geophysical Research Letters*, 39, L07803.

Fresnay, S. (2014). Prévisibilité des épisodes météorologiques á fort impact: sensibilité aux anomalies. PhD thesis. Université Paul Sabatier, Toulouse, France.

Giannakaki, P. and Martius, O. (2016) An object-based forecast verification tool for synoptic-scale Rossby waveguides. *Weather and Forecasting*, 31, 937–946.

Giorgi, F. (2006) Climate change hot-spots. *Geophysical Research Letters*, 33(8). https://doi.org/10.1029/2006GL025734.

Grams, C.M., Wernli, H., Boettcher, M., Čampa, J., Corsmeier, U., Jones, S.C., Keller, J.H., Lenz, C.-J. and Wiegand, L. (2011) The key role of diabatic processes in modifying the upper-tropospheric wave guide: a North Atlantic case-study. *Quarterly Journal of the Royal Meteorological Society*, 137, 2174–2193.

Grams, C.M., Binder, H., Pfahl, S., Piaget, N. and Wernli, H. (2014) Atmospheric processes triggering the central European floods in June 2013. *Natural Hazards and Earth System Sciences*, 14, 1691–1702.

Grams, C.M., Magnusson, L. and Madonna, E. (2018) An atmospheric dynamics perspective on the amplification and propagation of forecast error in numerical weather prediction models: a case study. *Quarterly Journal of the Royal Meteorological Society*, 144, 2577–2591.

Gray, S.L., Dunning, C.M., Methven, J., Masato, G. and Chagnon, J.M. (2014) Systematic model forecast error in Rossby wave structure. *Geophysical Research Letters*, 41, 2979–2987.

Grazzini, F. (2007) Predictability of a large-scale flow conducive to extreme precipitation over the western Alps. *Meteorology and Atmospheric Physics*, 95, 123–138.

Harrold, T.W. (1973) Mechanisms influencing the distribution of precipitation within baroclinic disturbances. *Quarterly Journal of the Royal Meteorological Society*, 99, 232–251.

Hewson, T.D., Magnusson, L., Breivik, O., Prates, F., Tsonevsky, I. and de Vries, J. (2014) Windstorms in Northwest Europe in late 2013. *ECMWF Newsletter*, 139, 22–28.

Hinrichsen, D. (1998) *Coastal waters of the world: trends, threats, and strategies*. Washington DC: Island Press.

Joos, H. and Forbes, R.M. (2016) Impact of different IFS microphysics on a warm conveyor belt and the downstream flow evolution. *Quarterly Journal of the Royal Meteorological Society*, 142, 2727–2739.

Kain, J.S. and Fritsch, J.M. (1993). Convective parameterization for mesoscale models: the Kain–Fritsch scheme, pp. 165–170 in The Representation of Cumulus Convection in Numerical Models. Emanuel, K.A., Raymond, D.J. (eds), Boston, MA: American Meteorological Society.

Keil, C., Chabert, L., Nuissier, O. and Raynaud, L. (2020) Dependence of predictability of precipitation in the northwestern Mediterranean coastal region on the strength of synoptic control. *Atmospheric Chemistry and Physics*, 20, 15851–15865.

Lebeaupin, C., Ducrocq, V. and Giordani, H. (2006) Sensitivity of torrential rain events to the sea surface temperature based on high-resolution numerical forecasts. *Journal of Geophysical Research: Atmospheres*, 111(D12). https://doi.org/10.1029/2005JD006541.

Madonna, E., Limbach, S., Aebi, C., Joos, H., Wernli, H. and Martius, O. (2014a) On the co-occurrence of warm conveyor belt outflows and PV streamers. *Journal of the Atmospheric Sciences*, 71, 3668–3673.

Madonna, E., Wernli, H., Joos, H. and Martius, O. (2014b) Warm conveyor belts in the ERA-Interim dataset (1979–2010). Part I: climatology and potential vorticity evolution. *Journal of Climate*, 27, 3–26.

Martínez-Alvarado, O., Madonna, E., Gray, S. and Joos, H. (2016) A route to systematic error in forecasts of Rossby waves. *Quarterly Journal of the Royal Meteorological Society*, 142, 196–210.

Martius, O., Zenklusen, E., Schwierz, C. and Davies, H.C. (2006) Episodes of Alpine heavy precipitation with an overlying elongated stratospheric intrusion: a climatology. *International Journal of Climatology*, 26, 1149–1164.

Martius, O., Schwierz, C. and Davies, H. (2008) Far-upstream precursors of heavy precipitation events on the Alpine south-side. *Quarterly Journal of the Royal Meteorological Society*, 134, 417–428.

Massacand, A.C., Wernli, H. and Davies, H.C. (1998) Heavy precipitation on the Alpine southside: an upper-level precursor. *Geophysical Research Letters*, 25, 1435–1438.

Massacand, A.C., Wernli, H. and Davies, H.C. (2001) Influence of upstream diabatic heating upon an Alpine event of heavy precipitation. *Monthly Weather Review*, 129, 2822–2828.

Nuissier, O., Joly, B., Joly, A., Ducrocq, V. and Arbogast, P. (2011) A statistical downscaling to identify the large-scale circulation patterns associated with heavy precipitation events over southern France. *Quarterly Journal of the Royal Meteorological Society*, 137, 1812–1827.

Pergaud, J., Masson, V., Malardel, S. and Couvreux, F. (2009) A parameterization of dry thermals and shallow cumuli for

mesoscale numerical weather prediction. *Boundary-Layer Meteorology*, 132. https://doi.org/10.1007/s10546-009-9388-0.

Piriou, J.-M., Redelsperger, J.-L., Geleyn, J.-F., Lafore, J.-P. and Guichard, F. (2007) An approach for convective parameterization with memory: separating microphysics and transport in grid-scale equations. *Journal of the Atmospheric Sciences*, 64, 4127–4139.

Ponzano, M., Joly, B., Descamps, L. and Arbogast, P. (2020) Systematic errors analysis of heavy precipitating events prediction using a 30-year hindcast dataset. *Natural Hazards and Earth System Sciences*, 20, 1369–1369.

Riemer, M., Jones, S.C. and Davis, C.A. (2008) The impact of extratropical transition on the downstream flow: an idealized modelling study with a straight jet. *Quarterly Journal of the Royal Meteorological Society*, 134, 69–91.

Rivière, G., Arbogast, P., Maynard, K. and Joly, A. (2010) The essential ingredients leading to the explosive growth stage of the European wind storm *Lothar* of Christmas 1999. *Quarterly Journal of the Royal Meteorological Society*, 136, 638–652.

Rivière, G., Arbogast, P., Lapeyre, G. and Maynard, K. (2012) A potential vorticity perspective on the motion of a mid-latitude winter storm. *Geophysical Research Letters*, 39(12). https://doi.org/10.1029/2012GL052440.

Rodwell, M.J., Magnusson, L., Bauer, P., Bechtold, P., Bonavita, M., Cardinali, C., Diamantakis, M., Earnshaw, P., Garcia-Mendez, A., Isaksen, L., Källén, E., Klocke, D., Lopez, P., McNally, A.P., Persson, A., Prates, F. and Wedi, N. (2013) Characteristics of occasional poor medium-range weather forecasts for Europe. *Bulletin of the American Meteorological Society*, 94, 1393–1405.

Schäfler, A. and Harnisch, F. (2015) Impact of the inflow moisture on the evolution of a warm conveyor belt. *Quarterly Journal of the Royal Meteorological Society*, 141, 299–310.

Schäfler, A., Dörnbrack, A., Wernli, H., Kiemle, C. and Pfahl, S. (2011) Airborne lidar observations in the inflow region of a warm conveyor belt. *Quarterly Journal of the Royal Meteorological Society*, 137, 1257–1272.

Schäfler, A., Craig, G., Wernli, H., Arbogast, P., Doyle, J.D., McTaggart-Cowan, R., Methven, J., Rivière, G., Ament, F., Boettcher, M., Bramberger, M., Cazenave, Q., Cotton, R., Crewell, S., Delanoë, J., Dörnbrack, A., Ehrlich, A., Ewald, F., Fix, A., Grams, C.M., Gray, S.L., Grob, H., Gross, S., Hagen, M., Harvey, B., Hirsch, L., Jacob, M., Kölling, T., Konow, H., Lemmerz, C., Lux, O., Magnusson, L., Mayer, B., Mech, M., Moore, R., Pelon, J., Quinting, J., Rahm, S., Rapp, M., Rautenhaus, M., Reitebuch, O., Reynolds, C.A., Sodemann, H., Spengler, T., Vaughan, G., Wendisch, M., Wirth, M., Witschas, B., Wolf, K. and Zinner, T. (2018) The North Atlantic waveguide and downstream impact experiment. *Bulletin of the American Meteorological Society*, 99, 1607–1637.

Schlemmer, L., Martius, O., Sprenger, M., Schwierz, C. and Twitchett, A. (2010) Disentangling the forcing mechanisms of a heavy precipitation event along the Alpine south side using potential vorticity inversion. *Monthly Weather Review*, 138, 2336–2353.

Selz, T. and Craig, G.C. (2015) Upscale error growth in a high-resolution simulation of a summertime weather event over Europe. *Monthly Weather Review*, 143, 813–827.

Sprenger, M. and Wernli, H. (2015) The LAGRANTO Lagrangian analysis tool – version 2.0. *Geoscientific Model Development*, 8, 2569–2586.

Turato, B., Reale, O. and Siccardi, F. (2004) Water vapor sources of the October 2000 Piedmont flood. *Journal of Hydrometeorology*, 5, 693–712.

Wernli, H. and Davies, H.C. (1997) A Lagrangian-based analysis of extratropical cyclones. I: the method and some applications. *Quarterly Journal of the Royal Meteorological Society*, 123, 467–489.

Wernli, H., Dirren, S., Liniger, M.A. and Zillig, M. (2002) Dynamical aspects of the life cycle of the winter storm *Lothar* (24–26 December 1999). *Quarterly Journal of the Royal Meteorological Society*, 128, 405–429.

Wernli, H., Paulat, M., Hagen, M. and Frei, C. (2008) SAL – a novel quality measure for the verification of quantitative precipitation forecasts. *Monthly Weather Review*, 136, 4470–4487.

Wernli, H., Hofmann, C. and Zimmer, M. (2009) Spatial forecast verification methods intercomparison project: application of the SAL technique. *Weather and Forecasting*, 24, 1472–1484.

Wilks, D.S. (2006) *Statistical Methods in the Atmospheric Sciences*. Cambridge, MA: Academic Press.

Winschall, A., Pfahl, S., Sodemann, H. and Wernli, H. (2012) Impact of North Atlantic evaporation hot spots on southern Alpine heavy precipitation events. *Quarterly Journal of the Royal Meteorological Society*, 138, 1245–1258.

Wirth, V., Riemer, M., Chang, E.K. and Martius, O. (2018) Rossby wave packets on the midlatitude waveguide-A review. *Monthly Weather Review*, 146, 1965–2001.

Zhang, F., Bei, N., Rotunno, R., Snyder, C. and Epifanio, C.C. (2007) Mesoscale predictability of moist baroclinic waves: convection-permitting experiments and multistage error growth dynamics. *Journal of the Atmospheric Sciences*, 64, 3579–3594.

How to cite this article: Binder, H., Rivière, G., Arbogast, P., Maynard, K., Bosser, P., Joly, B. *et al.* (2021) Dynamics of forecast-error growth along cut-off *Sanchez* and its consequence for the prediction of a high-impact weather event over southern France. *Quarterly Journal of the Royal Meteorological Society*, 147(739), 3263–3285. Available from: https://doi.org/10.1002/qj.4127